In situ study of the tensile deformation micro-mechanisms of semi-crystalline poly(ethylene terephthalate) films using synchrotron radiation X-ray scattering

Martin Donnay, Marc Ponçot, Jean-Philippe Tinnes, Thomas Schenk, Olivier Ferry, Isabelle Royaud

▶ To cite this version:

> Martin Donnay, Marc Ponçot, Jean-Philippe Tinnes, Thomas Schenk, Olivier Ferry, et al.. In situ study of the tensile deformation micro-mechanisms of semi-crystalline poly(ethylene terephthalate) films using synchrotron radiation X-ray scattering. Polymer, 2017, 117, pp.268-281. 10.1016/j.polymer.2017.04.043 . hal-03940267

HAL Id: hal-03940267

https://hal.science/hal-03940267

Submitted on 26 Jan 2023

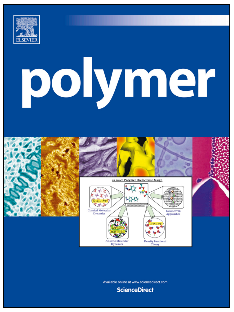

In situ study of the tensile deformation micro-mechanisms of semi-crystalline POLY(ETHYLENE terephthalate) films using synchrotron radiation X-ray scattering

Martin Donnay, Marc Ponçot, Jean-Philippe Tinnes, Thomas Schenk, Olivier Ferry, Isabelle Royaud

PII: S0032-3861(17)30421-4

DOI: 10.1016/j.polymer.2017.04.043

Reference: JPOL 19624

To appear in: *Polymer*

Received Date: 20 December 2016

Revised Date: 20 March 2017

Accepted Date: 17 April 2017

Please cite this article as: Donnay M, Ponçot M, Tinnes J-P, Schenk T, Ferry O, Royaud I, *In situ* study of the tensile deformation micro-mechanisms of semi-crystalline POLY(ETHYLENE terephthalate) films using synchrotron radiation X-ray scattering, *Polymer* (2017), doi: 10.1016/j.polymer.2017.04.043.

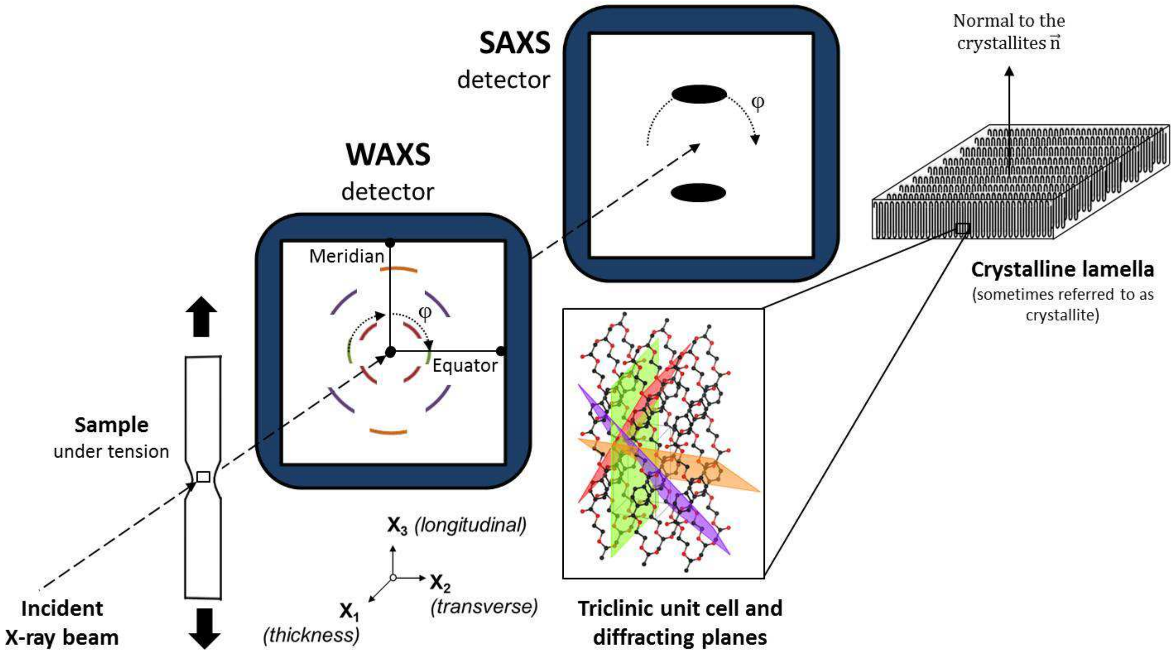
SAXS
detector
WAXS
detector
Meridian
φ
Equator
φ
Normal to the crystallites $\vec{n}$
Crystalline lamella
(sometimes referred to as crystallite)
Sample
under tension
Incident
X-ray beam
X_3 (longitudinal)
X_2 (transverse)
X_1 (thickness)
Triclinic unit cell and diffracting planes

IN SITU STUDY OF THE TENSILE DEFORMATION MICRO-MECHANISMS OF SEMI-CRYSTALLINE POLY(ETHYLENE TEREPHTHALATE) FILMS USING SYNCHROTRON RADIATION X-RAY SCATTERING

Martin Donnay*, Marc Ponçot, Jean-Philippe Tinnes, Thomas Schenk, Olivier Ferry, Isabelle Royaud

Institut Jean Lamour, UMR 7198 CNRS-Université de Lorraine, Parc de Saurupt CS 50840,
54011 Nancy Cedex, France

Keywords: Polyethylene terephthalate, films, tension, SAXS, WAXS

ABSTRACT

Wide- and small-angle X-ray scattering are used to perform *in situ* experiments with synchrotron radiation. The high X-ray intensity enabled the study of the deformation mechanisms of poly(ethylene terephthalate) semi-crystalline films under tension. Microstructural parameters such as crystallinity ratio, macromolecular orientation, long period, length, width and thickness of crystalline lamellae are measured. A new method to follow macromolecular orientation is detailed. In the elastic-viscoelastic region, lamellae rotate along the tensile axis without increase of orientation parameters. The plastic strain is initiated by crystallographic processes: crystal slip with (010)[001] and (010)[010] systems, flexural breaking of the longitudinal lamellae and separation of (010) planes in transverse lamellae,. The plastic flow is the continuation of these processes and the strengthening of the macromolecular orientation in both crystalline and amorphous phases. The shear forces applied to transverse lamellae rotating to a longitudinal orientation make them adopt a tilted shape.

---

* Corresponding author.
E-mail address: martin.donnay@univ-lorraine.fr

1. INTRODUCTION

Poly(ethylene terephthalate) (most commonly referred to as PET) is a semi-crystalline polyester mainly used for its good electrical insulation and mechanical properties, temperature resistance and permeability [1-3]. Having relatively slow crystallization kinetics, it became a first-class polymer as it can be processed into a large array of controlled microstructures. Biaxially-stretched PET films, similarly to the well-known trade name Mylar, have many applications in various fields such as electronics, packaging or medicine thanks to its biocompatibility. Depending on the process of biaxial stretching (simultaneous or sequential) and the machine and transverse draw ratios, these films can have very different microstructures and thus very different mechanical properties [4-12].

Microstructure and mechanical properties are indeed closely related, a change in the first will directly translate into a change in the latter. The deformation micromechanisms are responsible for the relation between the microstructure and the mechanical properties. Deformation micromechanisms are defined as the evolution (or adaptation) of the microstructure to an applied load or strain. Wide-Angle X-ray Scattering and Small-Angle X-ray Scattering (abbreviated WAXS and SAXS) are able to evidence a wide array of mechanisms and so have been extensively used for the past twenty years to study the deformation micromechanisms of semi-crystalline polymer under tension. This was possible thanks to the development of new-generation synchrotron light sources for materials' characterization which provide an excellent time resolution for *in situ* experiments [13, 14]. *In situ* experiments are necessary in order to accurately study the deformation mechanisms in polymers as opposed to *post mortem* experiments. A number of studies have shown modifications of the crystallinity ratio and amorphous phase orientation during stress relaxation of PET. This is a direct consequence of the formation and conversion of the transient mesophase formed during stretching above the glass transition temperature [15-18].

The tensile stretching of semi-crystalline polymers generates orientation of the macromolecules along the tensile direction both in the amorphous and crystalline phases. Macromolecular orientation is a fundamental aspect of the deformation mechanisms in polymers and so has been the main topic of multiple studies [19-23]. On the one hand, the orientation of the amorphous phase produces transitory phases that were evidenced in some polymers (e.g. in PET [24], polylactide [25], polypropylene [26, 27] and poly(trimethylene terephthalate) [28]) and are associated to the strain-induced crystallization at temperatures above the glass transition temperature [29, 30]. On the other hand, the strain transmitted to the crystalline lamellae generates distortions of the crystal lattice that were described earlier in polyethylene by Pope and Keller [31]. The consequence of such crystallographic processes are lamellar fragmentation [32, 33], crystalline phase transformations (e.g. in nylon 6 [34, 35] and polyvinylidene fluoride [36]) and martensitic-like phase transformation (e.g. in high-density polyethylene [14]). A number of papers have also used SAXS in order to measure the volume damage (or cavitation) occurring during the tensile stretching of semi-crystalline polymers [32, 37-41]. The technique gives access to the size and shape of the forming cavities which makes possible the determination of the intrinsic mechanical behavior of materials [41].

This paper aims at quantitatively study the deformations mechanisms in the elastic-viscoelastic and plastic domains of biaxially-stretched PET films under tension using synchrotron-radiation X-ray scattering. The combination of WAXS and SAXS enables a multi-scale analysis, from the crystallographic spacing distances up to the crystallite size (from a few Ångströms up to a few dozen nanometers). The evolution of the orientation of the polymer chains and the crystalline lamellae, crystallinity ratio, crystallite size and shape, spacing of specific crystallographic planes as a function of the applied true strain will be measured and discussed. The underlying mechanisms will be eventually identified and explained.

2. MATERIALS AND METHODS

2.1 Polyethylene terephthalate (PET) films

The materials investigated are semi-crystalline polyethylene terephthalate films having a thickness of 36µm. Their density is ρ=1.393 g.cm^{-3}. The temperature of the α-relaxation associated to the glass transition measured by dynamic mechanical analysis at 1 Hz is T_α=119 °C at the maximum of the loss tangent peak. The melting temperature measured by differential scanning calorimetry is T_m=255 °C at the maximum of the melting endotherm. The crystallinity ratio is χ_c=0.43, calculated with a melting enthalpy of a perfect crystal of 140 J/g [42]. The polymer chains in the crystallite phase are arranged in a triclinic lattice system having the following parameters: a=0.456 nm, b=0.594 nm, c=1.075 nm, α=98.5°, β=118°, γ=112° [43].

2.2 Sample preparation

The specimens are strips of 50 × 10 mm² with a round defect as shown on Figure 1(a). The defects located at the center of the specimens are symmetrical circular segments cut from the strips in order to produce a reduction of the cross-section and ensure the localization of the plastic strain in the scattering volume. The effective length is 30 mm. Two pieces of adhesive copper tape were placed at the center in order to measure the local strain from the video-recorded experiments. Because previous WAXS experiments showed an initial orientation of the chain segments in the crystalline phase, it was decided to cut samples along the longitudinal and transverse directions (parallel and perpendicular to the macromolecular orientation, respectively). The longitudinal and transverse samples will be noted LD and TD samples.

2.3 In-situ tensile tests

The samples were continuously strained at room temperature with a Kammrath & Weiss tensile micro-machine using a crosshead speed of 20 µm/s in the elastic-viscoelastic domain and 12 µm/s in the plastic domain. The crosshead speeds were calculated according to the true mechanical behavior at a constant true strain rate of 5.10^{-4} s^{-1} determined with the VidéoTraction™ system. This is a video-controlled tensile test during which the displacement of markers defining a Representative Volume Element (RVE) is recorded [44, 45]. The cross-head speed is adjusted in real-time as to obtain a constant true strain rate inside the RVE. For samples having a very low thickness-to-width ratio, the hypothesis are those of isochoric plane tension [46]: the transverse strain ε_{22} in the RVE is zero and the volumetric strain ε_v= ε_{11+} ε_{22+} ε_{33} is always null. As a consequence, the axial strain ε_{33} in the RVE is equal to the opposite of the normal strain ε_{11} in the RVE. The resulting axial load in the RVE is thus calculated using Equation 1:

$$\sigma_{33} = \frac{F}{S_0}\exp(\varepsilon_{33}) \qquad (1)$$

where F is the applied force and S_0 is the initial cross-section.

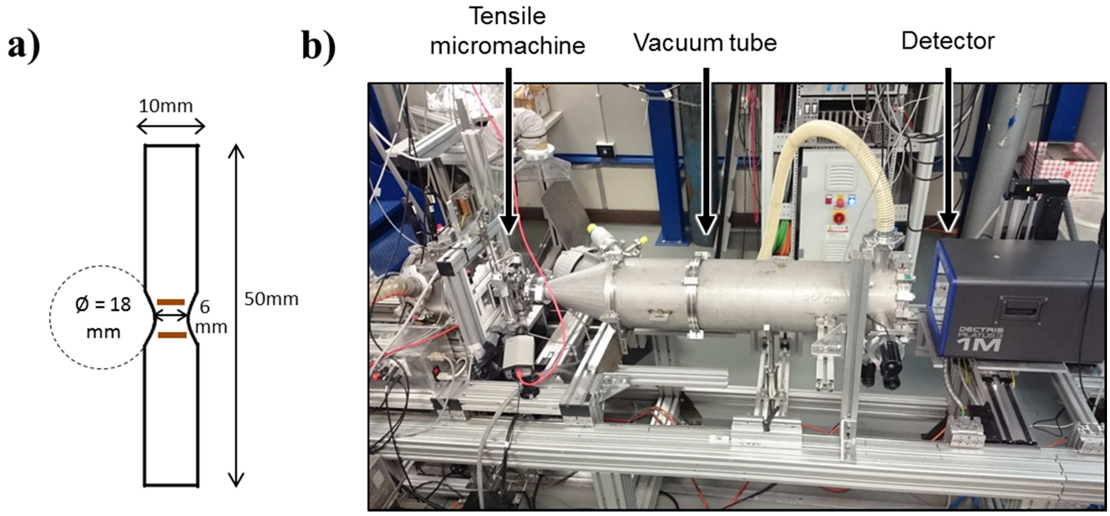

Figure 1 : (a) Schematic representation of the sample dimensions. (b) Photograph of the experimental setup in the SAXS configuration (SAXS beamline at Elettra Sincrotrone Trieste, Italy).

2.4 Wide/small-angle X-ray scattering with synchrotron radiation

The experiments were performed at the SAXS beamline of the Elettra Sincrotrone (Trieste, Italy). The energy of the incident X-ray beam was 8 keV corresponding to a wavelength of λ=0.154 nm. The spot size of the beam was 500 × 300 µm². The detector was a 2D Pilatus 3 1M with 981 × 1043 pixels², each pixel having a size of 172 × 172 µm². Frames were acquired every 3s with a 3s exposure time in order to obtain a pattern every 0.0015 of true strain. The readout time of the detector is 0.95 ms. Two detection modes were used (not simultaneously): Wide-Angle X-ray Scattering (WAXS) with a sample-to-detector distance of 177 mm and Small-Angle X-ray Scattering (SAXS) with a sample-to-detector distance of 1356 mm. The calibration of the q-scale in the SAXS signals (with silver behenate) and the 2θ-slace in the WAXS signals (with lanthanum hexaboride) were performed with the FIT2D software. The experimental setup in the SAXS configuration is shown in Figure 1(b). In the WAXS mode, the diffraction of the crystalline dense planes and the scattering of the amorphous phase are present between 10° and 35° in the 2θ-space. In the SAXS mode, the long periods (i.e. the regular stacking of crystalline and amorphous domains) are accessible between 0.78 nm^{-1} and 0.25 nm^{-1} in q-space.

2.5 X-ray scattering data analysis

Figure 2 is a schematic representation of the experimental setup containing the information necessary for the comprehension of the data analysis protocols detailed in this subsection.

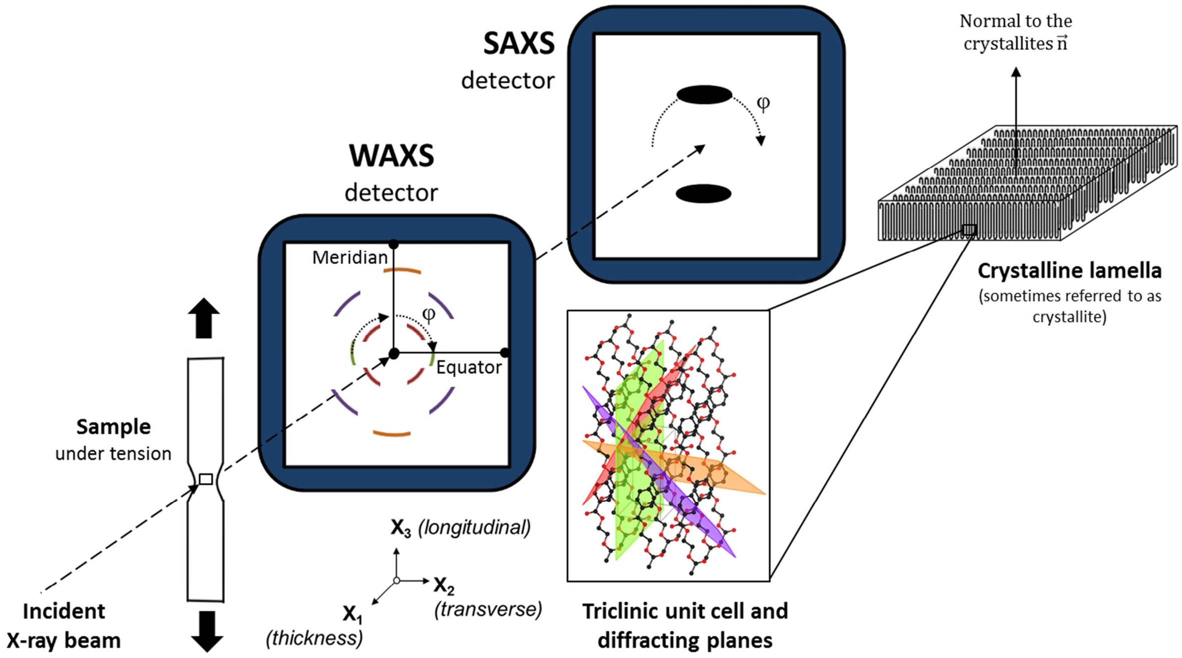

Figure 2 : Schematic representation of the experimental setup. The incident beam interacts with the polymer microstructure forming scattering patterns in the WAXS and SAXS ranges. The reflections shown here correspond to the longitudinal sample. An (X_1,X_2,X_3) Cartesian coordinates system is defined. The meridian/equator lines as well as the azimuthal-φ scans are displayed. The tensile axis is systematically set at an azimuthal angle φ=0. The normal to the crystallites $\vec{n}$ is defined as the vector perpendicular to the lamellae.

In the first place, the 2D WAXS and SAXS patterns were transformed into so-called "cake images" (i.e. polar transformation giving azimuth-vs-scattering-angle radial plots) using the FIT2D software [47, 48]. Due to the large amount of patterns recorded, MATLAB routines had to be written for the data analysis. The described procedures were successfully applied to all the patterns recorded as a function of strain.

2.5.1 Macromolecular orientation (WAXS)

The orientation distribution (scattered intensity vs azimuthal angle) of the (010) crystalline plane (centered around 17.8° in the 2θ-space) was recorded as well as the orientation distribution of the amorphous halo (centered around 21° in the 2θ-space) from the 2D WAXS cakes. The Hermans' orientation factor was chosen as a mean to quantitatively describe the orientation of both phases [49]. This factor noted $F_{\vec{X}/\vec{t}}$ depicts the relative orientation of a given crystallographic axis $\vec{X}$ against a fixed reference direction $\vec{t}$; here $\vec{t}$ is the tensile direction. Its mathematical expression is given in Equation 2.

$$F_{\vec{X}/\vec{t}} = \frac{3 < \cos^2\left(\alpha_{\vec{X}/\vec{t}}\right) > -1}{2} \qquad (2)$$

where : $< \cos^2\left(\alpha_{\vec{X}/\vec{t}}\right) > = \dfrac{\int_0^{\pi/2} I_{hkl} \times \cos^2\varphi \times \sin\varphi \times d\varphi}{\int_0^{\pi/2} I_{hkl} \times \sin\varphi \times d\varphi}$, I_{hkl} is the scattered intensity of the (hkl) plane at a given azimuthal angle φ.

The Hermans' orientation factors describing the orientation of the chain segments in the crystalline and in the amorphous phase will be noted $\mathrm{F}_{\overrightarrow{\mathrm{cr}}/\vec{\mathrm{t}}}$ and $\mathrm{F}_{\overrightarrow{\mathrm{am}}/\vec{\mathrm{t}}}$ respectively. $\overrightarrow{\mathrm{cr}}$ is the normal axis to the (010) planes and $\overrightarrow{\mathrm{am}}$ is the normal axis to the chain segments in the amorphous phase.

The remarkable values of $\mathrm{F}_{\vec{\mathrm{X}}/\vec{\mathrm{t}}}$ are listed in Table 1.

$< \cos^2(\alpha_{\vec{\mathrm{X}}/\vec{\mathrm{t}}}) >$	$\mathrm{F}_{\vec{\mathrm{X}}/\vec{\mathrm{t}}}$	**Texture**
0	-1/2	$\vec{\mathrm{X}}$ is perpendicular to $\vec{\mathrm{t}}$
1/3	0	Isotropic distribution of $\vec{\mathrm{t}}$ in space
1/2	1/4	Isotropic distribution of $\vec{\mathrm{X}}$ in the plane parallel to $\vec{\mathrm{t}}$
1	1	$\vec{\mathrm{X}}$ is parallel to $\vec{\mathrm{t}}$

Table 1 : Distinctive values of $\mathrm{F}_{\vec{\mathrm{X}}/\vec{\mathrm{t}}}$ used for the determination of the texture of the material with Hermans' orientation factor [49].

Another approach has been experimented in order to study the macromolecular orientation. In parallel to the Hermans' orientation factor, the orientation distribution tensor Ω has been calculated from the orientation distribution. The orientation distribution tensor is calculated using Equation 3 [50].

$$\Omega = \frac{\sum_{i=1}^{N} \mathrm{I}_{\mathrm{hkl}} \times \vec{\mathrm{r}_\imath} \otimes \vec{\mathrm{r}_\imath}}{\sum_{i=1}^{N} \mathrm{I}_{\mathrm{hkl}}} \tag{3}$$

where $\vec{\mathrm{r}_\imath} = \begin{pmatrix} \cos\varphi_i \\ \sin\varphi_i \end{pmatrix}$.

The eigenvalues λ_L and λ_T of the tensor were extracted and an anisotropy factor α was defined as [50]:

$$\alpha = 1 - \frac{\lambda_T}{\lambda_L} \tag{4}$$

The anisotropy factor ranges from 0 for an isotropic distribution up to 1 for a perfectly oriented material. The mathematical formulation is actually similar to Hermans' factor however in this case, the reference direction is not fixed but is taken as the direction at the maximum of the distribution. In brief, the Hermans' factor combines information about the sweep of the orientation (isotropic, slightly oriented, highly oriented…) and the direction of the orientation whereas the anisotropy factor only deals with the sweep of the orientation. Another information is necessary here, namely the main angle of orientation, which is the azimuthal angle at the maximum of the distribution. The tensile axis is centered at φ=0 degrees.

2.5.2 Crystallinity index (WAXS)

The 2D cake images of the WAXS patterns were integrated over the whole azimuthal angle and the resulting 1D diffractograms were deconvoluted. The shawrp peaks resulting from the diffraction of crystalline planes in the triclinic lattice were fitted with a Lorentzian distribution function. The halo resulting from the scattering of the amorphous phase was fitted with a Gaussian distribution function. The position, the full-width at half-maximum (FWHM) and the area of the deconvoluting functions were recorded. A crystallinity index χ_{ci} was thus calculated as the ratio of the area of the cumulated crystalline peaks over the total area of the signal following the Hermans-Weidinger method [51].

2.5.3 Lamellae dimensions (WAXS)

The same deconvolution procedure was performed on the equatorial and meridional axes (perpendicular and parallel to the tensile axis, respectively) of the WAXS patterns. The signal in both axes was integrated over an angle of 10 degrees (equatorial/meridional axis plus and minus 5 degrees) in order to measure characteristic features of crystals oriented along these particular axes.

The average planar spacing $d_{(010)}$ of the (010) plane was calculated for crystals oriented along the equatorial and meridional directions using the following formula (derived from Bragg's law):

$$d_{(010)} = \frac{\lambda}{2\,\sin\theta_{(010)}} \tag{5}$$

where λ is the wavelength of the incident X-ray beam (λ=0.154nm), $\theta_{(010)}$ is the scattering angle at the maximum of the peak.

The average crystallite width $L_{(010)}$ of the (010) plane was calculated for crystals oriented along the equatorial and meridional directions using Scherrer equation [52]. The instrumental broadening $\Delta 2\theta_{instr}$ was subtracted from the total width of the peak by plotting the width of the peak vs 2θ for the calibrant and a Lorentzian distribution shape.

$$L_{(010)} = \frac{K \times \lambda}{\Delta 2\theta_{(010)} \,.\, \cos\theta_{(010)}} \tag{6}$$

where K=0.9, $\Delta 2\theta_{(010)}$ is the FWHM of the (010)-plane diffraction peak such as $\Delta 2\theta_{(010),total} = \Delta 2\theta_{(010)} + \Delta 2\theta_{(010)instr}$.

2.5.4 Long period (SAXS)

The long period L_p was calculated from the SAXS patterns as a function of the azimuthal angle using the following formula:

$$L_p = \frac{2\pi}{q_{max}} \tag{7}$$

where q_{max} is the position of the maximum of the scattering halo in the SAXS patterns

The thickness of the lamellae t_{lam} (i.e. the size of the lamellae in the chains direction) can be estimated by combining the long period and the crystallinity index:

$$t_{lam}=L_p \times \chi_{ci} \tag{8}$$

The orientation distribution of the long period (at scattering vector q_{max}) was recorded from the SAXS patterns. The Hermans' orientation factor was also used to quantify the orientation of the normal of the crystallites $\vec{n}$ relative to the tensile axis. The factor will be noted $F_{\vec{n}/\vec{t}}$ with n being the normal to the crystallites as shown in Figure 2.

3. RESULTS

3.1 True mechanical behavior

The mechanical behaviors at room temperature of the films in the longitudinal and transverse directions (noted LD and TD) are shown in Figure 3.

The mechanical behaviors were recorded in real-time during the *in situ* experiments. They can be decomposed into two regions: an elastic-viscoelastic region ranging from $\varepsilon=0$ to $\varepsilon=0.018$ and a plastic domain from $\varepsilon=0.018$ until break. The viscoelastic-to-plastic transition will be represented on the forthcoming figures by a dashed line at a true strain of $\varepsilon=0.018$. The elastic-viscoelastic domain has a mostly linear shape. The plastic deformation of these materials in both directions exhibits a strain hardening process. The anisotropy is only clearly noticeable in this plastic domain: the slope of the strain hardening process is much lower in the transverse direction than in the longitudinal direction.

In the longitudinal direction, the yield point was measured at 91 MPa, the slope of the strain hardening at 550 MPa and the true stress and strain at break at 265 MPa and $\varepsilon=0.32$ respectively. In the transverse direction, the yield point was measured at 86 MPa, the slope of the strain hardening at 269 MPa and the true stress and strain at break at 219 MPa and $\varepsilon=0.52$ respectively.

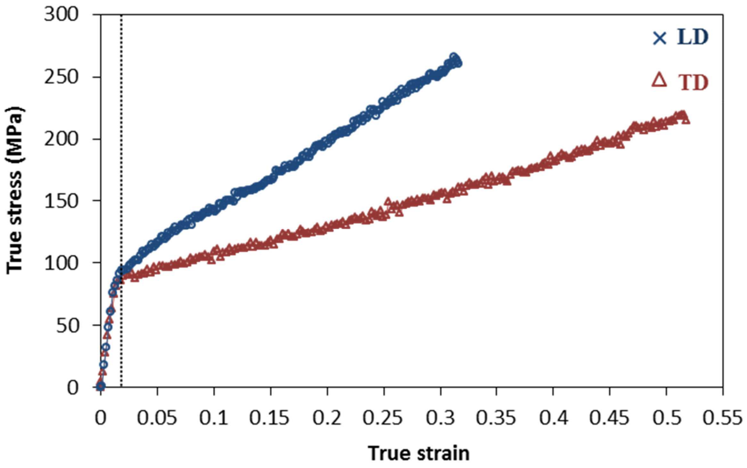

Figure 3 : Comparison of the true mechanical behavior of LD and TD samples. They were acquired along the procedure detailed in section 2.3.

3.2 WAXS/SAXS patterns analysis

3.2.1 WAXS patterns

Figure 4 presents the evolution of the 2D WAXS patterns of the LD sample at several true strains. The diffraction rings were indexed from the triclinic crystal cell of polyethylene terephthalate. Several dense planes were found to meet Bragg's condition including the $(0\bar{1}1)$ the (010), $(\bar{1}12)$ and $(\bar{1}03)$ planes. The $(11\bar{3})$ reflection is visible in the corners of the patterns but do not span over the entire azimuthal angle. The integrated 1D diffractogram is shown in Figure 5.

Upon stretching, the reflections corresponding to the amorphous phase and the (010) planes concentrate on the equator. The (010) planes are directly parallel to the chain segments in the crystalline phase. The $(\bar{1}03)$ planes have a normal oriented close to the chain axis with an offset of 20 degrees. As a consequence, the scattered intensity of the $(\bar{1}03)$ reflection concentrates close to the meridian. These are signs of macromolecular orientation along the tensile axis (vertical in the patterns).

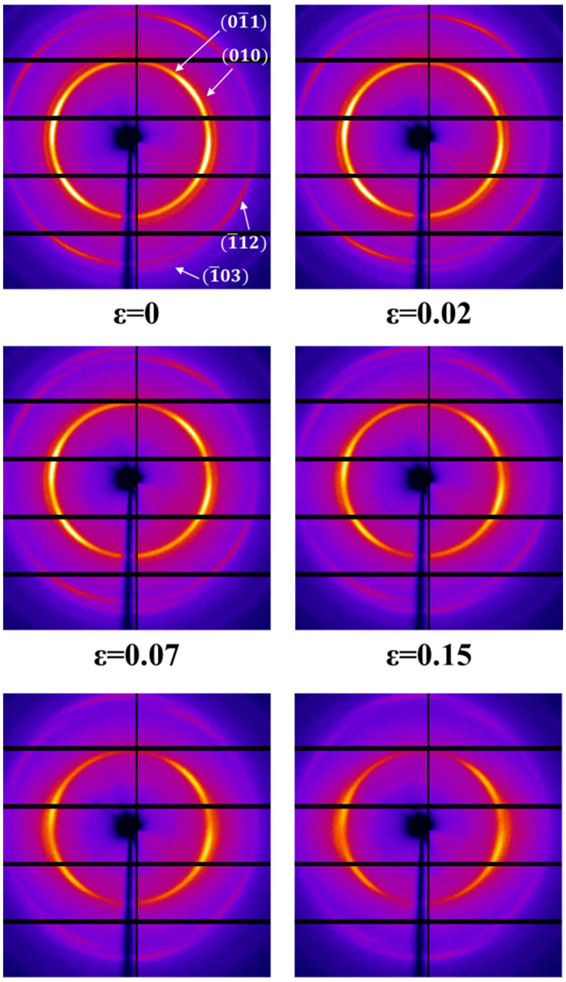

ε=0 ε=0.02

ε=0.07 ε=0.15

ε=0.23 ε=0.31

Figure 4 : Evolution of the 2D WAXS patterns of the longitudinal sample as a function of the applied true strain. The stretching direction is vertical.

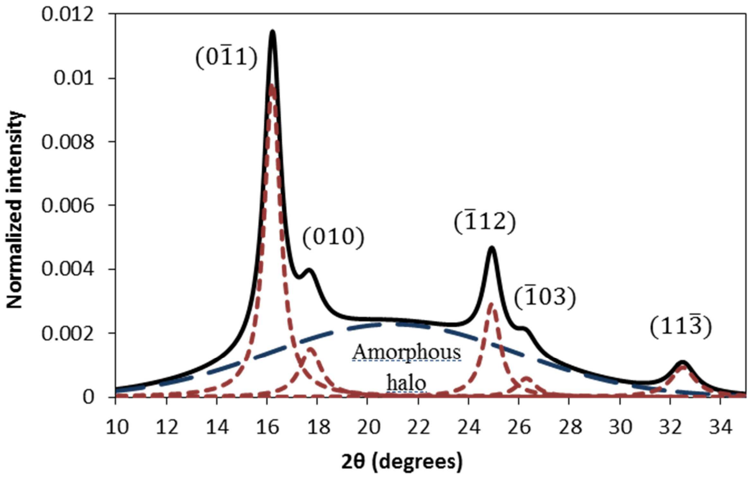

Figure 5 : WAXS diffractogram (integrated 2D pattern over 180°) of the unstrained material showing the deconvoluted diffracting peaks and amorphous halo. The diffracting planes are labelled with their corresponding Miller indices (hkl).

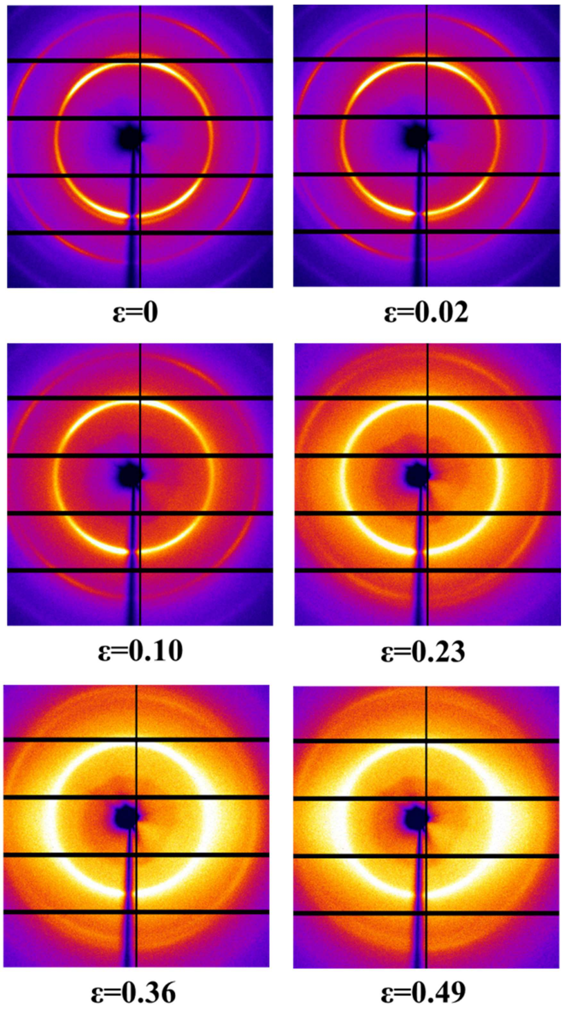
ε=0 **ε=0.02**

ε=0.10 **ε=0.23**

ε=0.36 **ε=0.49**

Figure 6 : Evolution of the 2D WAXS patterns of the transverse sample as a function of the applied true strain. The stretching direction is vertical.

The evolution of the 2D WAXS patterns for the transverse sample is shown in Figure 6. The authors emphasizes that the brightness and contrast were set to identical levels for all the strain states and for both the LD and TD samples. During plastic deformation, the patterns exhibit significant differences from the LD sample. After the onset of plastic strain, the transverse orientation rotates to an isotropic state. The overall intensity later concentrates on the equator, which results from the superimposition of the intensity of the (010) reflection and the amorphous scattering, in a similar fashion as the LD sample. The scattering halo representative of the amorphous phase gains significant intensity for the TD sample.

The evolution of the crystallinity index measured from 1D diffractograms (see Figure 5) has been displayed on Figure 7. On both samples, the crystallinity index significantly decreases with strain, starting from an initial value of χ_{ci}=0.42. For the LD sample, the index remains constant after the onset of plastic deformation up to ε=0.15. The crystallinity index then decreases to χ_{ci}=0.37 before failure. For the TD sample, the amount of crystal phase diminishes after the onset of plastic strain. A crystallinity index of χ_{ci}=0.28 is measured before failure.

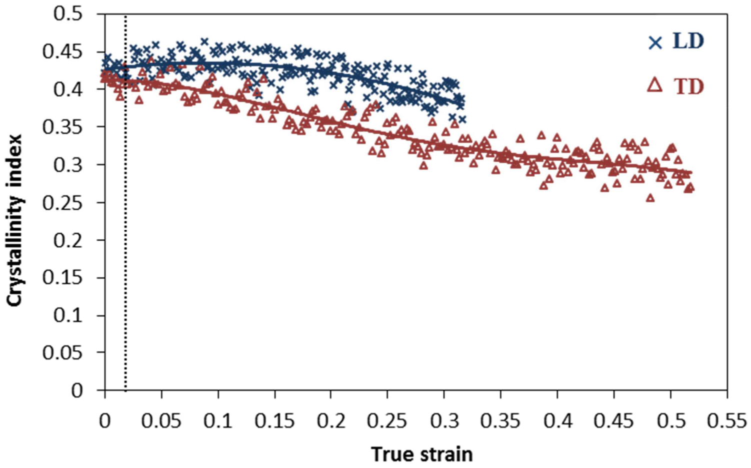

Figure 7 : Evolution of the crystallinity index as a function of true strain for the longitudinal and transverse samples.

3.2.2 SAXS patterns

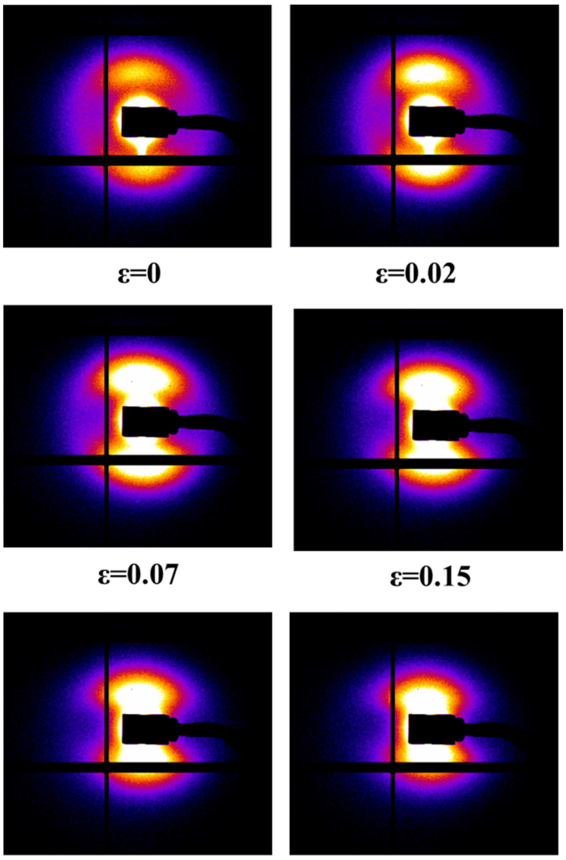

ε=0 ε=0.02

ε=0.07 ε=0.15

ε=0.23 ε=0.28

Figure 8 : Evolution of the 2D SAXS patterns of the longitudinal sample as a function of the applied true strain. The stretching direction is vertical.

The SAXS patterns recorded for the LD and TD samples at several strains are shown in Figure 8 and Figure 9 respectively. At the unstrained state, an anisotropic scattering characteristic of a unidimensional stacking can be seen on both samples, with a maximum intensity on the meridian for the LD sample and on the equator for the TD sample. This scattering is typically associated with the long period in semi-crystalline polymers, which is the unidimensional stacking of crystalline lamellae and interlamellar amorphous domains. During the stretching of the LD sample, the scattering gradually gains intensity during the elastic-viscoelastic and plastic domain. This is linked to the increase of the density difference between the crystalline and the interlamellar amorphous phase. In the plastic domain, the scattering associated to the long period gets closer to the center of the pattern, indicating an increase of the long period. On the equator, the intensity notably decreases indicating the reorientation of the normal to the lamellae $\vec{n}$ parallel to the tensile direction.

A different process occurs during straining of the TD sample. The reorientation of the lamellae operates after the onset of plastic strain. The maximum intensity later concentrates on the meridian to disappear into the beamstop and becomes indiscernible at ε=0.36. It is interesting to note that the SAXS pattern has a 4-point scattering (visible at ε=0.10) which reveals a particular shape adopted by the crystallites. This will be discussed into more details in section 4.3.2 of this article.

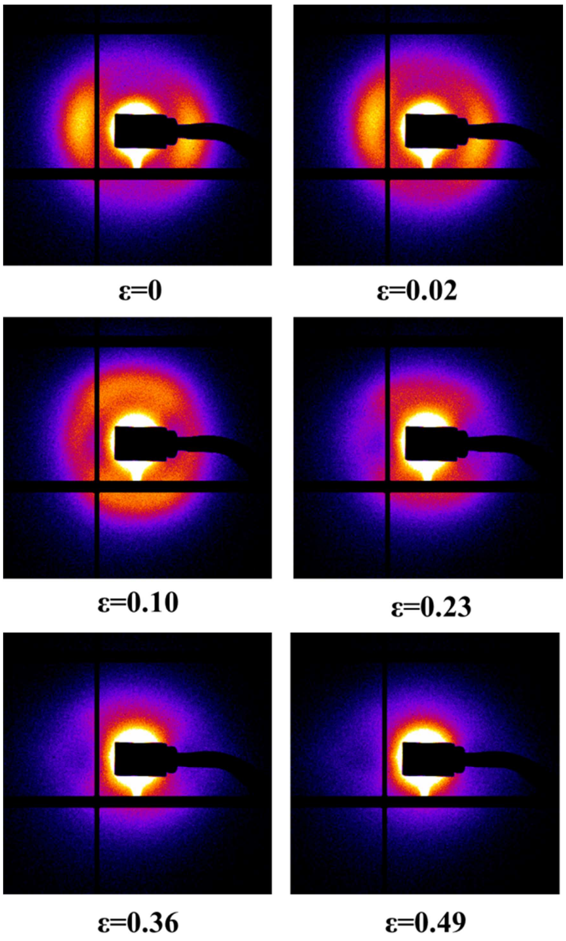

Figure 9 : Evolution of the 2D SAXS patterns of the transverse sample as a function of the applied true strain. The stretching direction is vertical.

3.3 Macromolecular orientation (WAXS)

The orientation distribution can be quantitatively described using the Hermans' orientation factor as well as the anisotropy factor combined with the main angle of orientation as explained in section 2.5.1.

3.3.1 Macromolecular orientation in the amorphous phase (Figure 10)

The chain segments in the amorphous phase have an initial isotropic orientation ($F_{\overrightarrow{am}/\vec{t}}=0$). The macromolecular orientation of the amorphous phase exhibits very similar trends for both the LD and TD samples. $F_{\overrightarrow{am}/\vec{t}}$ has a generally linear evolution, weaker in the elastic-viscoelastic domain than in the plastic domain. Similarly, the anisotropy factor has an initial value close to zero (isotropic). It is however strictly stable in the elastic-viscoelastic domain (Figure 10(b)). The main angle calculated for the amorphous phase evolves rapidly in the very first instants to reach asymptotically the tensile direction (Figure 10(c)).

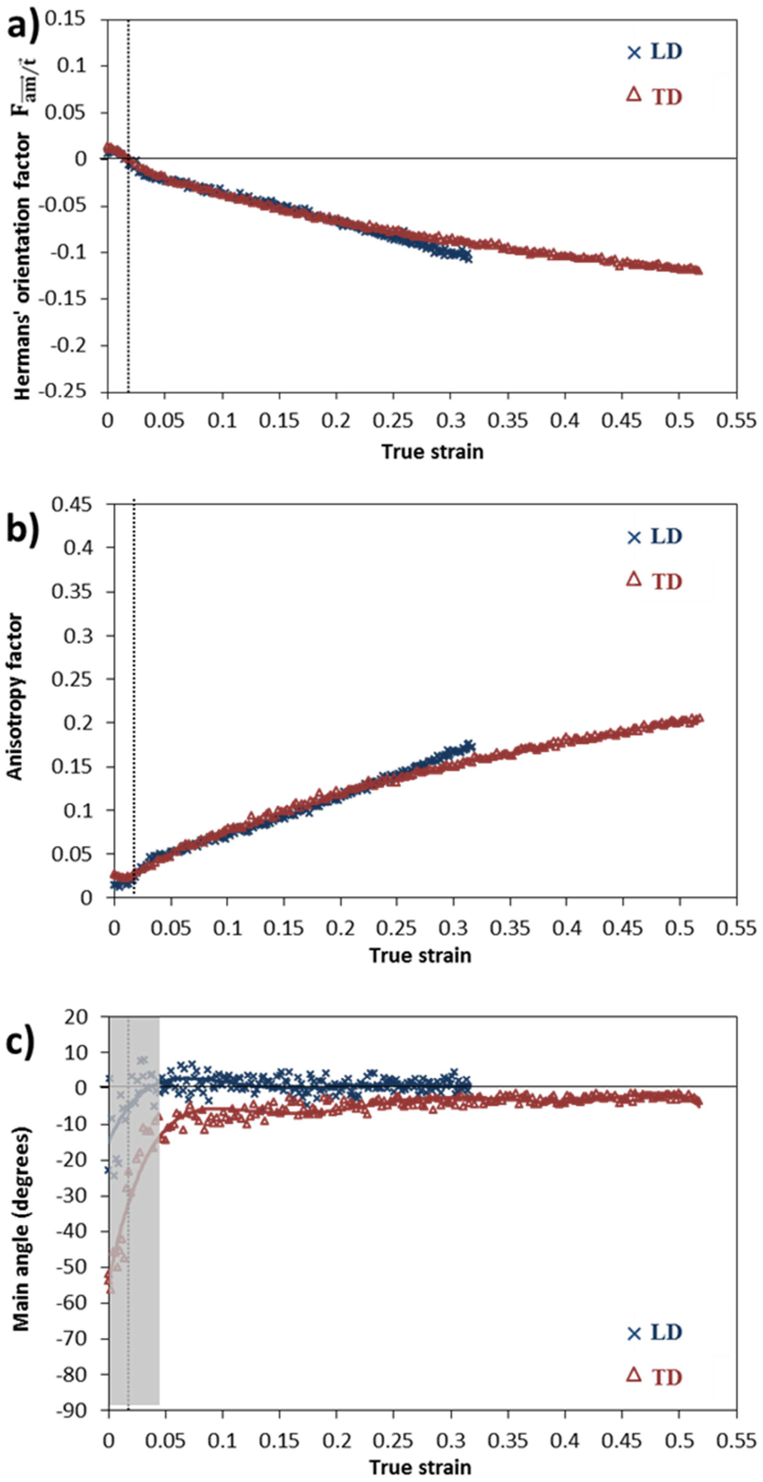

Figure 10 : Evolution of the macromolecular orientation parameters of the amorphous phase as a function of true strain for the longitudinal and transverse samples: (a) Hermans' orientation factor $F_{\overrightarrow{am}/\vec{t}}$ (b) anisotropy factor and (c) main angle. The measurement of the main angle has very little significance when the orientation is low. As a consequence, the first values of the main angle were grayed until the anisotropy factor reaches an arbitrary value of 0.05.

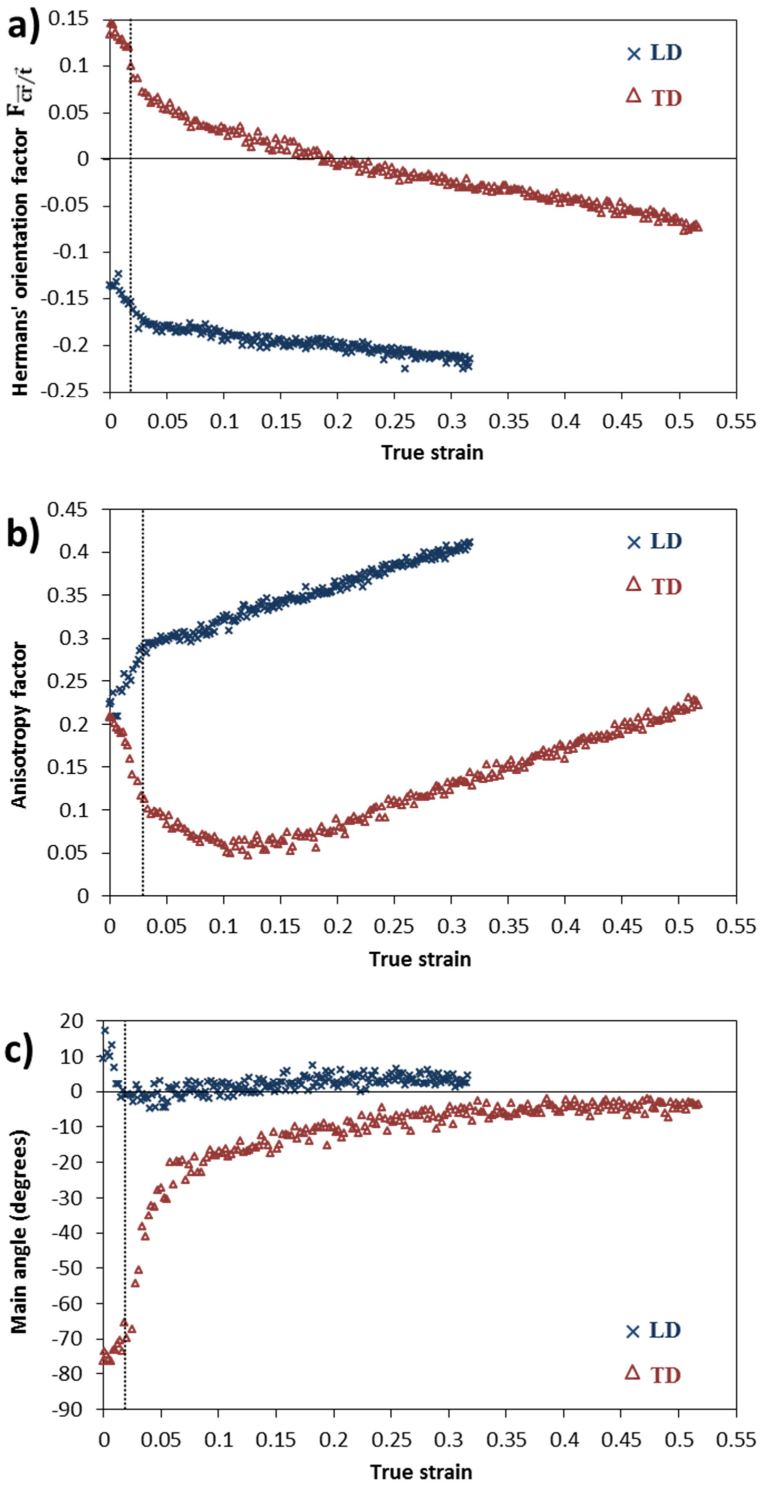

Figure 11 : Evolution of the macromolecular orientation parameters of the crystalline phase as a function of true strain for the longitudinal and transverse samples: (a) Hermans' orientation factor $F_{\overrightarrow{cr}/\vec{t}}$ (b) anisotropy factor and (c) main angle.

3.3.2 Macromolecular orientation in the crystalline phase (Figure 11)

In the LD, the distribution of the chain segments in the crystals is initially anisotropic with a Hermans' orientation factor $F_{\overrightarrow{cr}/\vec{t}}$ of -0.14 (Figure 11(a)) and an anisotropy factor of

0.22 (Figure 11(b)). The main angle is tilted with an offset of 10° relative to the tensile axis although it must be noted that it was intended to be along the tensile axis (Figure 11(c)). The evolution of $F_{\overrightarrow{cr}/\vec{t}}$ and α is steep in the elastic-viscoelastic domain then softens in the plastic domain. The chain segments in the lamellae rotate along the tensile axis in the very first instants of straining as indicated by the main angle (see Figure 11(c)).

In the transverse direction, $F_{\overrightarrow{cr}/\vec{t}}$ decreases through the zero value, sign of a loss of orientation to an isotropic state. The chain segments in the crystalline phase later rotate along the tensile axis. The anisotropy factor pictures the same process. It shows at first a decreasing trend in the elastic-viscoelastic domain and the beginning of the plastic domain at a true strain of ε=0.11 before increasing. The main angle of orientation is constant in the elastic-viscoelastic domain but rises significantly in the first instants of plastic deformation before reaching asymptotically the tensile axis.

3.4 Crystallites orientation (SAXS)

Figure 12 displays the orientation distribution of the normal to the crystallites $\vec{n}$ at various true strains for the LD and TD samples respectively. It corresponds to the azimuthal intensity profile measured from the SAXS patterns. The corresponding Hermans' orientation factors $F_{\vec{n}/\vec{t}}$ were calculated and plotted in Figure 13.

In the LD, the orientation distribution of the crystallites is anisotropic which is in good agreement with the anisotropic macromolecular orientation measured in the crystalline phase from the WAXS patterns. As a consequence, the chain segments in the lamellae are oriented strictly parallel to $\vec{n}$. After the onset of plastic strain, the distribution adopts a particular bell shape with an intensity plateau from -25° to 25° centered on the tensile direction. This particular distribution is held until failure. Moreover, the intensity of the profiles significantly decreases upon stretching. This is a consequence of the disappearance of scattering elements in this range of q-space. In other words, the long period increases and no longer can be resolved due to the limited sample-to-detector distance. Despite this decrease in intensity, $F_{\vec{n}/\vec{t}}$ reaches lower values indicating the orientation of $\vec{n}$ along the tensile axis. It is interesting to point that $F_{\vec{n}/\vec{t}}$ and $F_{\overrightarrow{cr}/\vec{t}}$ have a very similar evolution as a function of strain.

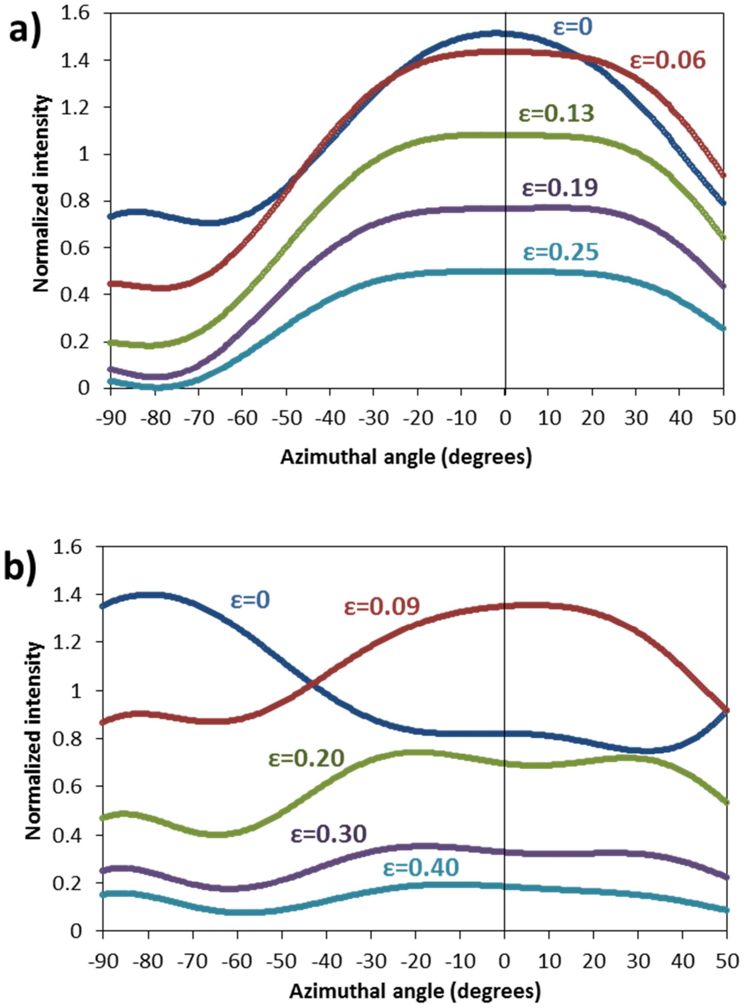

Figure 12 : Orientation distribution (intensity profile vs azimuthal angle profiles) for the normal to the crystallites $\vec{n}$ at various true strains. (a) Longitudinal sample. (b) Transverse sample. All the intensities were normalized with the average intensity of the distribution at the initial state.

In the TD, the initial anisotropic distribution of the normal to the crystallites $\vec{n}$ is centered at approximately -80°, similarly to the macromolecular orientation. The distribution shifts to the tensile axis and adopts a bimodal profile. This bimodal profile is well pronounced: two maximums are distinguishable at -25° and +25°. $F_{\vec{n}/\vec{t}}$ also characterizes the reorientation of $\vec{n}$ along the tensile axis in the elastic-viscoelastic domain. Care must be taken while looking at $F_{\vec{n}/\vec{t}}$. Unlike the WAXS patterns, the scattering vanishes into the beamstop because the size of the scattering elements becomes too large to be seen in the patterns. As a consequence, the Hermans' factor $F_{\vec{n}/\vec{t}}$ depicts the orientation of scattering elements only in this precise range of q-value. The anisotropy factors and main angles are not shown here as their evolution is falsified by this limitation of q-range.

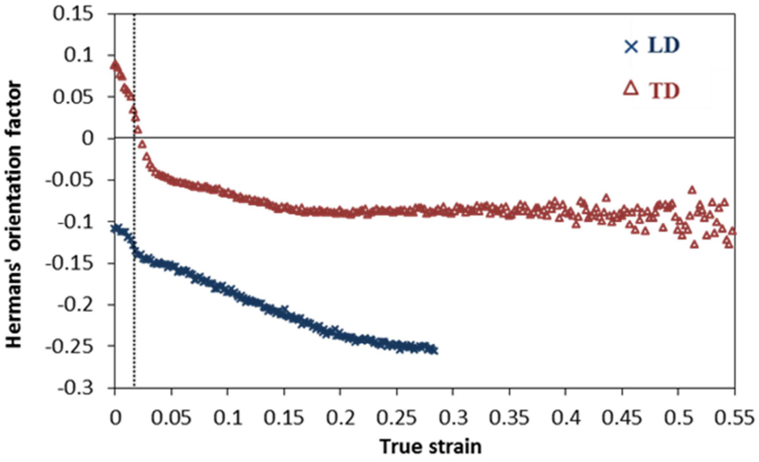

Figure 13 : Evolution of the Hermans' orientation factor $F_{\vec{n}/\vec{t}}$ as a function of true strain for the longitudinal and transverse samples. $\vec{X}$ is $\vec{n}$, the vector normal to the crystallites.

3.5 Crystallites size

3.5.1 Crystallites width $L_{(010)}$ (WAXS)

Figure 14 displays the evolution of the crystallites average width $L_{(010)}$ calculated with the Scherrer equation (see Equation 6). This value corresponds to the length of the crystallites in the direction perpendicular to the (010) plane (perpendicular to the macromolecules in the plane of the film). It was applied to crystallites having a (010) reflection on the equator or on the meridian only. The validity of this calculation with the Scherrer equation is discussed in section 4.3.1. It was not possible to measure accurately the values for the LD sample on the meridian because the intensity of the reflection is initially low and becomes lower with strain (because of the orientation of the chains along the tensile axis). As a consequence, the meridional profile in the LD sample has a gradually lower intensity with strain which produces an inaccurate measurement.

The crystallites average width on the equator has a similar evolution for both samples. The initial width between 11nm and 13nm remains stable in the elastic-viscoelastic domain but decreases after the onset of plastic strain, down to 3nm before break. On the meridian, the crystallites width is reduced considerably at the end of the elastic-viscoelastic strain and at the onset of plastic strain, reaching a value of 3nm from ε=0.03.

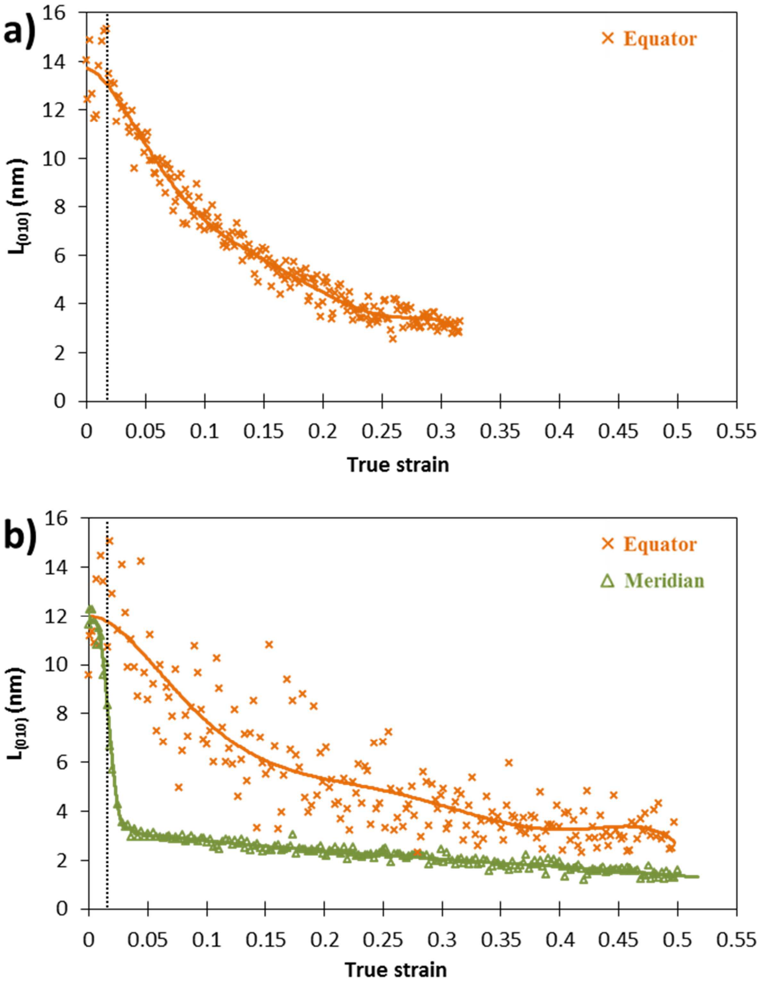

Figure 14 : Evolution of the crystallites average width $L_{(010)}$ (calculated with the Scherrer equation from the (010) peak width) on the equator and meridian as a function of true strain. (a) Longitudinal sample. (b) Transverse sample.

3.5.2 Long period and crystallites thickness t_{lam} (SAXS)

The long period is plotted against the azimuthal angle in Figure 15 for the LD sample at several true strains. The same measurement was not possible for the TD sample because, as it was pointed out in Figure 9, the long period is not visible during most of the plastic domain. Initially, the long period is 12nm along the tensile axis and smaller (8nm) in the perpendicular axis. This value increases with increasing true strain along the tensile axis and remains constant along the perpendicular axis. There appears to be a crossover point at an azimuthal angle of approximately -60°. The long period remains constant below this angle while it increases otherwise.

A value of the thickness of the crystallites t_{lam} of 5.6 nm was calculated from the long period using Equation 8. Even though the long period increases with strain along the tensile axis, this is only due to the stretching of the interlamellar amorphous phase. As a consequence, the initial value of t_m is assumed to be constant throughout the test.

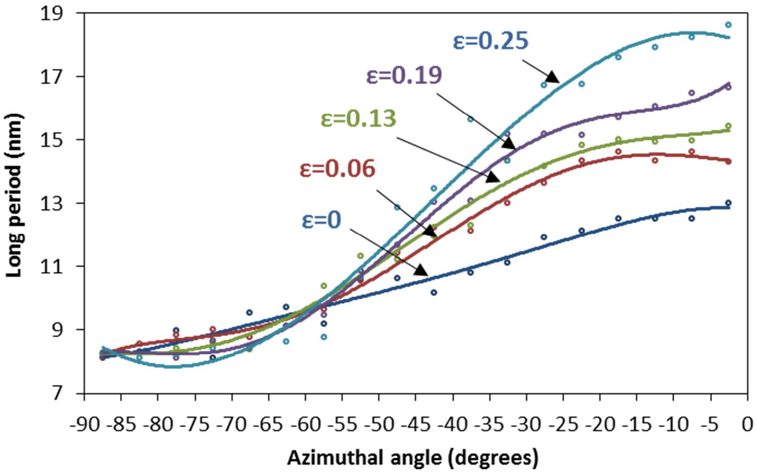

Figure 15 : Evolution of the long period vs azimuthal angle for the longitudinal sample at various strain states. The tensile axis is set at φ=0 degrees.

3.5.3 Crystallites length L_{lam}

Due to the initial texture of the samples, the (100) reflections are not available and cannot be used to determine the length of the lamellae (i.e. the dimension along the thickness of the films). This was overcome by using the $(\bar{1}12)$ reflection and, similarly to the (010) plane, calculate the size of the lamellae in the normal direction $L_{(\bar{1}12)}$. A transformation matrix was then used to make a projection of the vector normal to the $(\bar{1}12)$ plane (that is in the (a,b,c) triclinic coordinate system) into a (X_1,X_2,X_3) Cartesian coordinate system. As a consequence, the length of the lamellae L_{lam} can be deduced from $L_{(\bar{1}12)}$, $L_{(010)}$ and t_{lam} by projecting vectors in the Cartesian coordinate system. A representation of a lamella and the corresponding dimensions is shown in Figure 16.

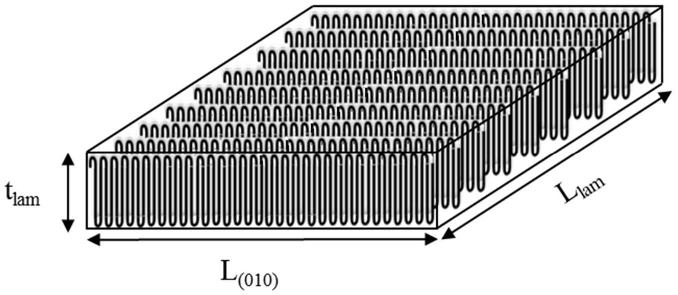

Figure 16 : Schematic representation of a lamella and the corresponding dimensions that are measured in this paper.

The evolution of L_{lam} for the LD sample is shown in Figure 17. The lamellae have an initial length of 60 nm. This value remains constant in the elastic-viscoelastic domain and suddenly falls to 15 nm right after the onset of plastic strain. The length of the crystallites keeps decreasing below 10 nm during plastic deformation.

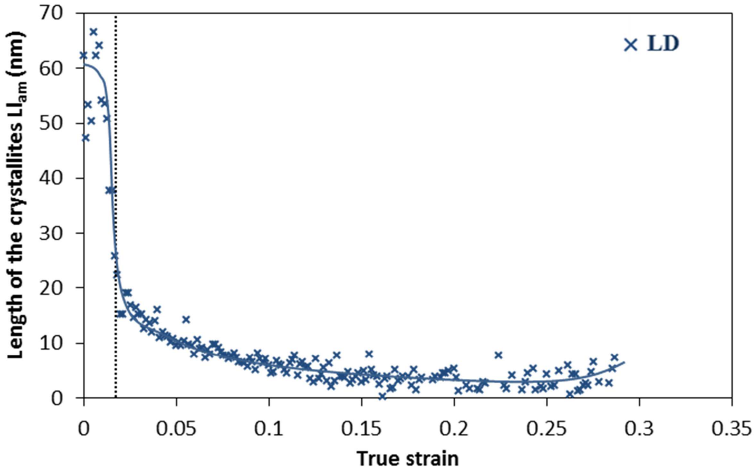

Figure 17 : Evolution of the length of the crystallites (dimension of the lamellae along the thickness of the samples) for the longitudinal sample as a function of true strain.

4. DISCUSSION

4.1 Initial texturing

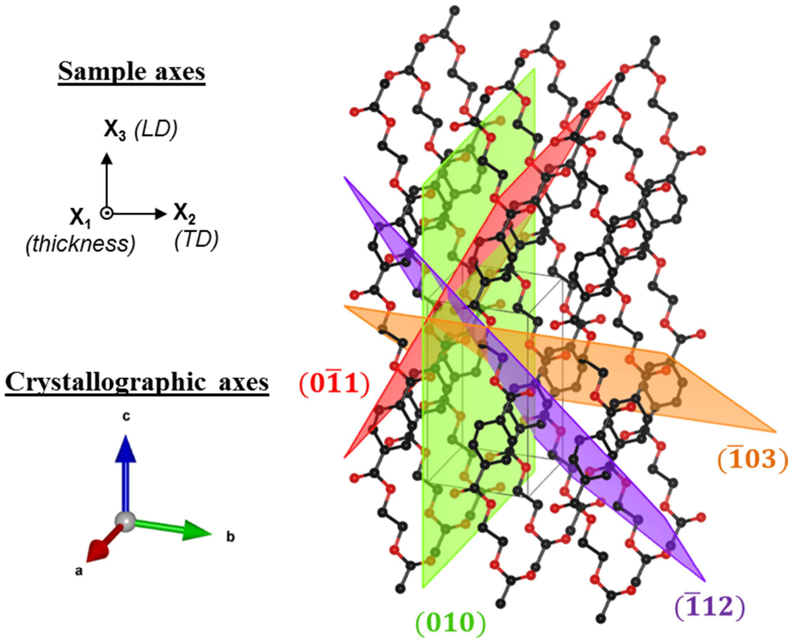

Figure 18 : Schematic representation of the triclinic crystal cell of polyethylene terephthalate and the corresponding crystallographic planes as viewed from the incident beam. These pictures were made with the VESTA 3 software [53].

In the unstrained state, the PET films have a particular texture due to their processing conditions. The (100) crystallographic planes are invisible in the WAXS patterns although they are very intense for non-textured materials [54]. Indeed, they do not fulfill the Bragg's conditions when the incident beam is perpendicular to the film plane. They are lying exactly perpendicular to the incident beam (normal incidence) hence they are parallel to the film plane. The aromatic rings of the PET macromolecules are inscribed in the (100) plane. It has been reported previously that the aromatic cycles of PET processed into films align parallel to the film plane due to their own shape [6, 10, 21]. This texture is represented in Figure 18. The crystal lattice is seen as from the point of view of the incident beam. The longitudinal direction is defined as the direction of the polymer chains because the macromolecular orientation was measured using the (010) reflection. As a consequence, the normal to the (010) plane lies exactly perpendicular to the chain segments.

4.2 Elastic-viscoelastic strain domain (strain from 0 to 0.018) and onset of plastic strain

The mechanical behaviors of the materials presented in Figure 3 are typical of oriented semi-crystalline PET films [4]. The strain hardening process takes place directly after the onset of plastic deformation. It is interesting to note that the behaviors of the LD and TD samples are extremely similar up to the yield point and only separate afterwards. The mechanisms involved in the elastic-viscoelastic domain are consequently not significantly affected by the anisotropic crystallites distribution. While a small number of frames (10-12 frames) are available during the elastic-viscoelastic deformation of the samples, the processes taking place in this region can still be analyzed.

4.2.1 Longitudinal sample

There is an increase of orientation of the chain segments in the crystal phase along the tensile axis (Figure 11) consistent with an increase of orientation of the normal of the crystallites $\vec{n}$ parallel to the tensile axis. There is also a significant rise in the long period which is attributed to the stretching of the interlamellar amorphous phase (IAP). As the IAP stretches along the tensile axis, the stress is transferred to the crystallites whose normal rotates parallel to the axis. As a consequence, this process affects both the long period and the orientation of the chain segments in the crystals. From Figure 10, the orientation of the IAP does not change during the elastic-viscoelastic deformation. Only a slight change in main angle (Figure 10(c)) is visible. This indicates that the chain segments in the IAP rotate but do not stretch significantly. Only a very small portion of the IAP, namely tie molecules, is responsible for this pull on the crystallites and consequently reorientation. Tie molecules are segment of macromolecules belonging both to the IAP and the crystallites. They connect two crystallites through the IAP. They play an important role in the cohesiveness of the phases and in the mechanical resistance while representing only a small amount of the macromolecular volume [55]. This also explains the important load required during the elastic-viscoelastic deformation because tie molecules are caught in physical entanglements [38].

Not only do tie molecules are responsible for the rotation of the lamellae but also for the strains applied to crystallographic planes as shown on Figure 19. The figure shows the evolution of the interplanar spacing of the (010) crystallographic planes reflecting on the meridian and the equator as a function of true strain. Even though it was not possible to make accurate measurements for the meridional reflections in the LD sample, it is hypothesized that the trend is similar to the TD sample in the range of strain discussed here. The number of crystallographic planes scattering on the meridian is indeed smaller for the LD sample. However, they will undergo the same deformation processes based on their relative orientation to the tensile axis. The resulting strain is almost non-existent for crystallographic planes reflecting on the equator. Only a small decrease in the planar spacing attributed to a Poisson’s effect is visible. For the meridional (010) reflection, the strain is large and increases sharply in the elastic-viscoelastic domain up to a plateau starting at $\varepsilon=0.04$. This adds to the significant load required for elastic-viscoelastic deformation because intermolecular forces are strong in the crystals. This plateau exhibited by the (010) planar spacing is supposed to be the maximum spacing for this crystallographic plane before separation. From Figure 14, the width of the lamellae is unaffected by the elastic-viscoelastic strain but is significantly reduced after the onset of plastic deformation for meridional reflections. This is the consequence of the separation of the lamellae at the (010) crystallographic planes. Moreover, the length of the crystallites L_{lam} (Figure 17) is also reduced after the yield point. The mechanism responsible for the reduction of L_{lam} is the crystallographic slip of the (100) planes.

These two crystallographic processes, lamellar separation of the (010) planes and crystal slip of the (100) planes, result in the activation of the plastic flow. The local stress requirement for these processes to set off is very close. Due to the limited time resolution of these experiments, it is impossible to conclude on which process is set off first.

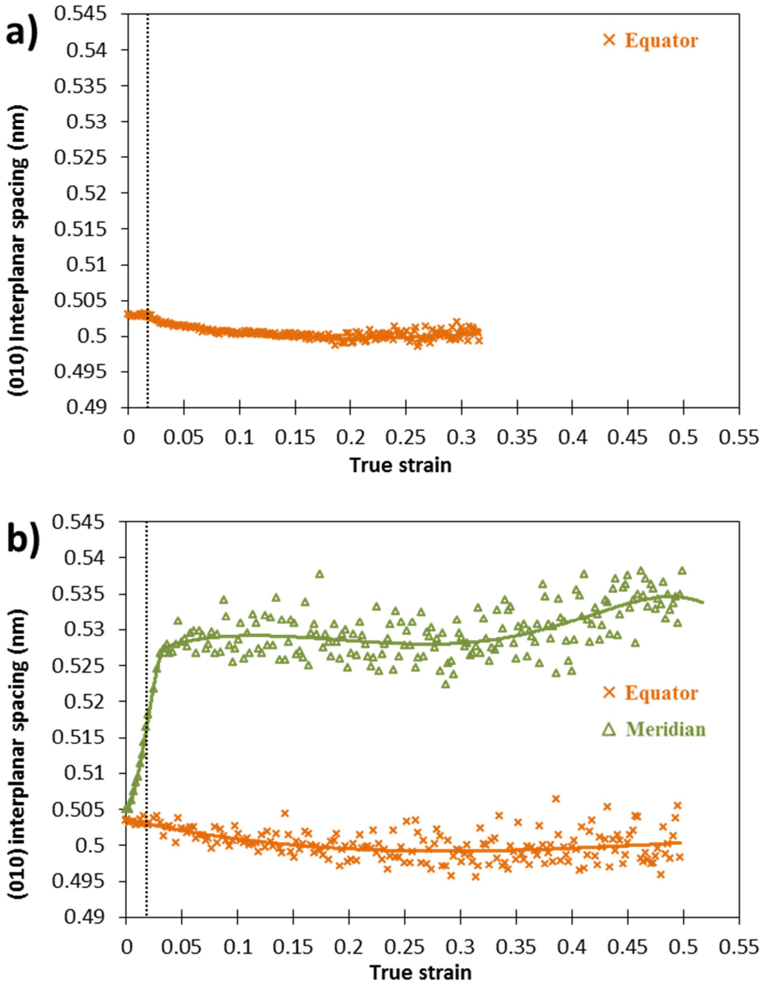

Figure 19 : Evolution of the (010) interplanar spacing for reflections lying on the equator and meridian as a function of true strain. (a) Longitudinal sample. (b) Transverse sample.

These observations are consistent with the current knowledge on the activation of plastic strain in semi-crystalline polymers. In polyethylene and polypropylene, it has been reported on multiple occasions about the dependency of the yield point on the initial lamellae thickness [56-59]. The accepted model for this phenomenon is the activation of screw dislocations with a Burgers vector parallel to the chain axis [60]. The formation of such dislocations leads rapidly to the fragmentation of the lamellae because of the relatively small thickness of the lamellae (5.6nm, which corresponds to five repeating units in the c crystallographic axis).

4.2.2 Transverse sample

The conclusions are very similar to the LD sample. As it was already mentioned, the mechanical behaviors in this range of strain are extremely similar for the two samples indicating that the mechanisms at stake are also similar. Nevertheless, a notable difference is the reorientation of the lamellae. While the majority of the lamellae in the LD sample already had their normal parallel to the tensile axis, the majority of the lamellae must rotate their normal along the tensile axis. This process already begins in the elastic-viscoelastic region but does not seem to produce a significant shift in the true stress-strain curves before the yield point.

4.3 Plastic strain domain (strain from 0.018 to failure)

4.3.1 Longitudinal sample

According to the previous discussion, the plastic flow is activated as soon as crystallographic processes are activated in the crystalline lamellae as a consequence of the local strains applied by tie molecules. One is the lamellar separation of crystallites having their chains perpendicular to the tensile axis due to the pull of the (010) crystallographic planes. Another is the crystallographic slip of (100) planes. Hence a large decrease in the width and length of the crystallites is measured around the yield point.

The calculation of the dimensions of the lamellae using the Scherrer equation requires additional specification. Three distinct phenomena produce the broadening of diffraction peaks: instrumental broadening, inhomogeneous strains and finite size effects, the latter being estimated by the Scherrer equation. First, the instrumental broadening has been calculated from the pattern recorded using a calibration component (see section 2.4). It is affected by multiple factors associated to the experimental setup such as the wavelength distribution, the spot size, the active diffracting volume or misalignments in the diffractometer. Secondly, inhomogeneous strains also originate from multiple sources, the most important being crystallites subjected to different strains (due to their orientation relative to the tensile axis) and crystal defects (dislocations…). The first source is here being minimized because the sizes are calculated for crystallites scattering on the equator OR on the meridian. Crystal defects are often neglected but this cannot be confirmed with absolute certainty. At the initial state, it is assumed that the amount of crystals defects is negligible. However during stretching, the crystals undergo substantial load which is very likely to create such defects. Nonetheless dislocations in crystallites of small dimensions are unstable and lead to the fragmentation of the crystal during further stretching.

The reduction of $L_{(010)}$ on the equator (Figure 14) is much softer than on the meridian and could be assigned to the reorientation of yet-fragmented crystallites that separated while oriented in the transverse direction. The (010)[001] slip system has been reported non-active and thus cannot account for the decrease of $L_{(010)}$ on the equator [61]. The only active slip systems that were reported for PET crystals are (100)[001] and (100)[010]. Due to the initial texture of the PET films, these slip systems were not available for direct analysis. Indeed they would lead to a reduction of the length of the crystallites but the (100) plane does not fulfill the Bragg's condition. The calculation of the length of the crystallites is however possible using the $(\bar{1}12)$ reflection projected into Cartesian coordinates (see section 2.5 for more details). This revealed active (100)[001] and (100)[010] slip systems taking place at the onset of plastic strain.

Nonetheless, another mechanism can account for the decrease of the width of longitudinal lamellae, namely the flexural breaking [62]. Even though it is not possible to attest directly for the occurrence of this mechanism, the shape of the curve in Figure 14 gives strong evidence. Several changes of slope were measured at $\varepsilon=0.018$, $\varepsilon=0.10$ and $\varepsilon=0.24$. The size of the crystals is divided by two at each change of slope which is consistent with a bending fragmentation mechanism rather than the reorientation of yet-fragmented crystallites.

Finally, the combination of all these mechanisms results in lamellae with highly reduced length and width at $\varepsilon=0.05$. The lamellar fragmentation mechanisms highlighted in this paper are schematized in Figure 20.

The sudden fragmentation of the crystals that takes place at the elastic-to-plastic transition leads to a rise of the macromolecular mobility of the IAP. This is characterized by a sudden increase of the anisotropy factor of the amorphous phase (Figure 10(b)) at the onset of plastic strain. The plastic flow above $\varepsilon=0.05$ comprises the strengthening of the orientation of both the amorphous and crystalline phase with the long period increasing along the tensile axis. A small loss of crystallinity index (approx. 5%) has been measured that can be attributed to a melting mechanism caused by chain unravelling by shear forces that typically takes place at large strains [63].

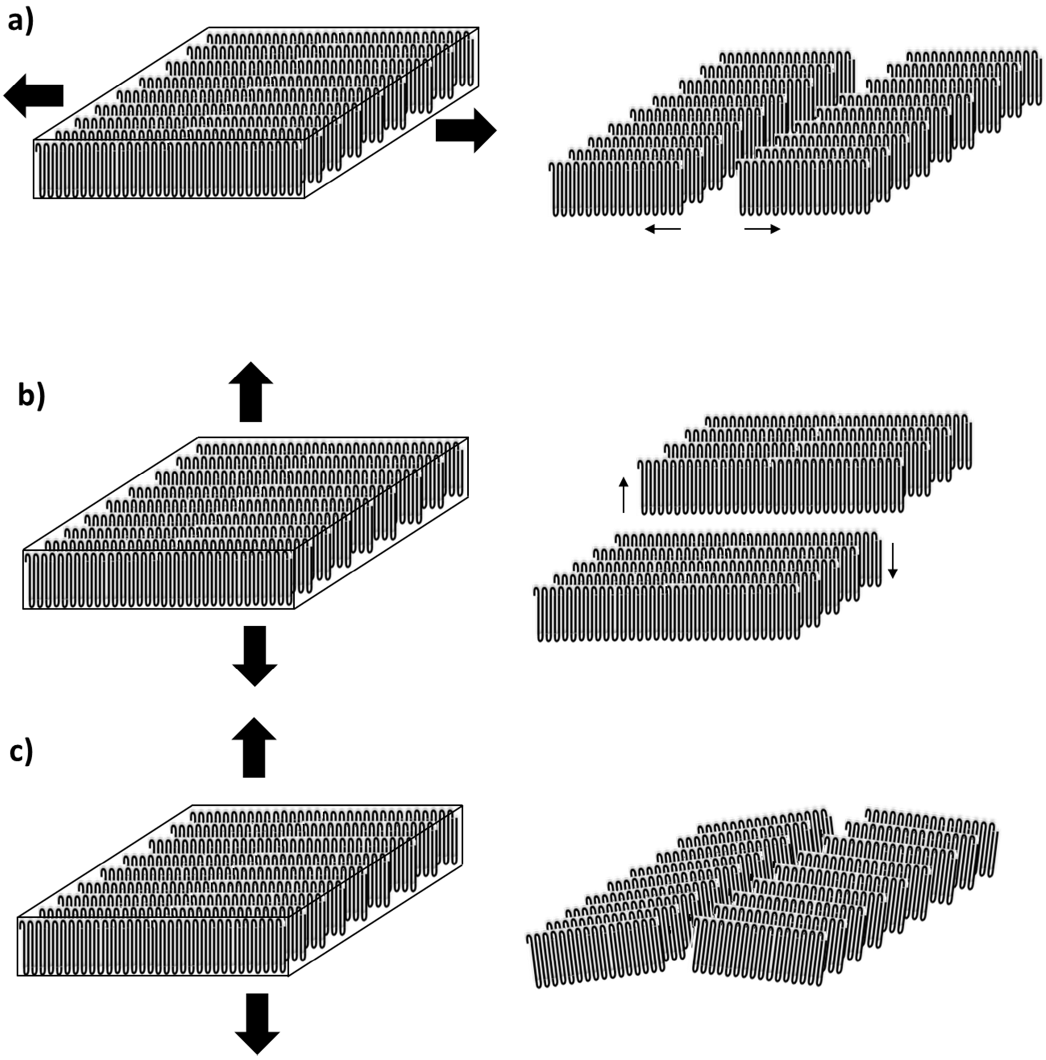

Figure 20 : Schematics of the lamellar fragmentation mechanisms highlighted in the discussion. (a) Lamellar separation at the (010) planes for transverse lamellae. (b) Crystallographic slip with a (010)[001] slip system. (c) Flexural breaking of longitudinal lamellae. The bold arrows indicate the tensile direction.

4.3.2 Transverse sample

The process of plastic deformation appears very different from the LD sample as shown by the mechanical behaviors (Figure 3), the WAXS and SAXS patterns (Figure 6, Figure 9) or the evolution of the crystallinity index (Figure 7). The crystallinity index decreases after the elastic-to-plastic transition. The transverse lamellae are more abundant in this sample and undergo an unravelling mechanism. This unravelling could be associated to a succession of lamellar separations in those crystals [63]. Moreover, the evolution of the crystal width on the equator (Figure 14) has a very similar shape as the LD sample, also pointing towards the flexural breaking of the lamellae. The crystals are indeed subjected to the same deformation processes only depending on their own orientation relative to the tensile axis [64]. The exact same plastic strain mechanisms take place in both samples. The difference originates from the amount (or volume) of chain segments affected by one mechanism or another. Only the most predominant ones give the highest signal and can be analyzed according to the initial orientation of the majority of the lamellae.

The process of crystallites reorientation from transverse to longitudinal is active in the elastic-viscoelastic domain and in the beginning of the plastic domain (Figure 10(c), Figure 11(c)). There is a significant disorientation of the crystallites as they rotate to align their normal parallel to the tensile direction while the amorphous phase follows a very similar trend as the LD sample. As soon as the majority of those crystallites are oriented accordingly, a positive slope in the anisotropy factor is initiated around ε=0.10. The slope of the strain hardening process is here much lower than for the longitudinal sample. The required load is indeed naturally lower at any given strain because the amount of longitudinal crystallites is always smaller.

The bimodal distribution of $\vec{n}$ appears at ε=0.10 (Figure 12(b)). The main angle of the chain segments in the crystal phase is, as a consequence, different from the main angle of the normal of the crystallites and a four-point SAXS pattern is obtained (Figure 9). This has been reported by multiple authors and point towards a distorted shape of the lamellae [65-68]. While the chain segments in the crystallites are perfectly oriented along the tensile axis, $\vec{n}$ is titled by an angle between 30° and 10° relative to the tensile axis. A schematic of a tilted lamella is shown in Figure 21. This was observed to a lesser extent in the LD sample. The intensity plateau seen in Figure 12a is likely due to the superimposition of the bimodal distribution seen for the TD sample (caused by tilted lamellae) with the unimodal distribution (caused by straight lamellae). This leads to the conclusion that tilted lamellae are formed through the shear forces applied during the reorientation process from a transverse to a longitudinal orientation.

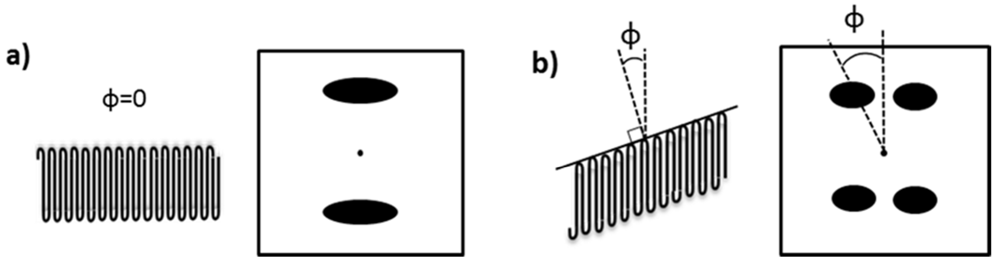

Figure 21 : Schematic of the shape of the lamellae and the corresponding SAXS patterns: (a) Straight lamella. (b) Tilted lamella.

5. CONCLUSION

WAXS and SAXS analyses reveal to be an excellent combination for the *in-situ* study of deformation micromechanisms of semi-crystalline polymers. The determination of the crystals dimensions and the orientation parameters proved effective in explaining the observed events. During the elastic-viscoelastic strain domain, the mechanism was not affected by the initial anisotropy of the samples as both samples (transverse or longitudinal orientation at the initial state) exhibited the same behavior. It is characterized by an elongation of tie molecules, pulling on the crystallites and deforming them as well as the rotation of the macromolecules along the tensile axis, both in the amorphous and crystalline phase. It seems that the plastic flow is triggered as soon as the local load on the lamellae is sufficient to activate crystallographic processes in the crystallites. Two of these processes were identified: lamellar separation at the (010) planes for lamellae oriented perpendicular to the tensile axis and crystal slip with (100)[001] and (100)[010] slip systems. In the longitudinal sample, the plastic flow mainly consists of the repeated fragmentation of the crystallites coupled with the intensification of the orientation of both phases along the tensile direction. In the transverse sample, the complete reorientation of the lamellae from a transverse to a longitudinal orientation allows for more ductility. It also shows the presence of a significant amount of tilted lamellae, i.e. lamellae having a non-zero angle between their normal and the segments of macromolecules they are made of, which is the consequence of the shear forces applied during reorientation.

All previously-mentioned plastic strain micromechanisms take place in both samples but only the most prominent can be assessed in each sample. Crystallites having a transverse orientation exist in the longitudinal sample and there is a very good chance that these crystallites will adopt a tilted shape as they reorientate even though it was not visible in the patterns. In order to fully characterize the deformation micromechanisms of a material, it is thus necessary to study both orientations.

ACKNOWLEDGEMENTS

The authors would like to thank the SAXS beamline at Elettra Sincrotrone Trieste and the CERIC-ERIC research infrastructure.

Funding: this work was supported by the Alsace and Lorraine regions and the Urban Community of Greater Nancy.

REFERENCES

[1] W. Reddish, "The dielectric properties of poly-ethylene terephthalate (terylene)," *Trans. Faraday Soc.,* vol. 46, pp. 459-475, 1950.

[2] K. Ravindranath and R. A. Mashelkar, "Polyethylene terephthalate—I. Chemistry, thermodynamics and transport properties," *Chem. Eng. Sci.,* vol. 41, pp. 2197-2214, 1986.

[3] A. S. Michaels, W. R. Vieth and J. A. Barrie, "Diffusion of Gases in Polyethylene Terephthalate," *J. Appl. Phys.,* vol. 34, pp. 13-20, 1963.

[4] Y. Rao, J. Greener, C. A. Avila-Orta, B. S. Hsiao and T. N. Blanton, "The relationship between microstructure and toughness of biaxially oriented semicrystalline polyester films," *Polymer,* vol. 49, pp. 2507-2514, 2008.

[5] A. Viswanathan, D. R. Riff and W. Adams, "An Investigation of Structure-Property Correlations in Polyethylene Terephthalate Films," Polymer Branch, Air Force Materials Laboratory, 1976.

[6] H. Chang, J. M. Schultz and R. M. Gohil, "Morphology of biaxially stretched poly(ethylene terephthalate) films," *J. Macromol. Sci. Part B Phys,* vol. 32, pp. 99-123, 1993.

[7] G. H. Kim, C.-K. Kang, C. G. Chang and D. W. Ihm, "Molecular Orientation Angle of Biaxially Stretched Poly(ethylene terephthalate) films," *Eur. Polym. J.,* vol. 33, pp. 1633-1638, 1997.

[8] C. J. Heffelfinger and P. G. Schmidt, "Structure and Properties of Oriented Poly(ethylene terephthalate) films," *J. Appl. Polym. Sci.,* vol. 9, pp. 2661-2680, 1965.

[9] R. M. Gohil, "Morphology-Property Relationships in Oriented Pet Films: A role of In-Plane Crystalline Orientation Distribution on the Film Properties," *J. Appl. Polym. Sci.,* vol. 48, pp. 1635-1648, 1993.

[10] M. Cakmak, J. E. Spruiell and J. L. White, "Small Angle and Wide Angle X-Ray Pole Figure Studies on Simultaneous Biaxially Stretched Poly(Ethylene Terephthalate) (PET) Films," *Polymer Engineering and Science,* vol. 27, pp. 893-905, 1987.

[11] A. C. Middleton, R. A. Duckett, I. M. Ward, A. Mahendrasingam and C. Martin, "Real-time FTIR and WAXS studies of drawing behavior of poly(ethylene terephthalate) films," *J. Appl. Polym. Sci.,* vol. 79, pp. 1825-1837, 2001.

[12] H.-N. Vu, C. Gauthier, O. Lame and J.-Y. Cavaillé, "Influence of annealing treatments on the essential work of fracture of biaxially drawn poly(ethylene terephthalate)," *Polym. Int.,* vol. 61, pp. 1094-1100, 2011.

[13] D. J. Hugues, A. Mahendrasingam, W. B. Oatway, E. L. Heeley, C. Martin and W. Fuller, "A simulataneous SAXS/WAXS and stress-strain study of polyethylene deformation at high strain

rates," *Polymer,* vol. 38, pp. 6427-6430, 1997.

[14] M. F. Butler, A. M. Donald, W. Bras, G. R. Mant, G. E. Derbyshire and A. J. Ryan, "A Real-Time Simultaneous Small- and Wide-Angle X-ray Scattering Study of In-Situ Deformation of Isotropic Polyethylene," *Macromolecules,* vol. 28, pp. 6383-6393, 1995.

[15] D. J. Blundell, D. H. Mac Kerron, Fuller W., A. Mahendrasingam, C. Martin, R. J. Oldman, R. J. Rule and C. Riekel, "Characterization of strain-induced crystallization of poly(ethylene terephthalate) at fast draw rates using synchrotron radiation.," *Polymer,* vol. 37, pp. 3303-3311, 1996.

[16] D. J. Blundell, A. Mahendrasingam, C. Martin, W. Fuller, D. H. Mac Kerron, J. L. Harvie, R. J. Oldman and C. Riekel, "Orientation prior to crystallization during drawing of poly(ethylene terephthalate).," *Polymer,* vol. 41, pp. 7793-7802, 2000.

[17] R. Matthews, "The effects of stress relaxation on the structure and orientation of tensile drawn poly(ethylene terephthalate).," *Polymer,* vol. 41, pp. 7139-7145, 2000.

[18] A. K. Oultache, X. Kong, C. Pellerin, J. Brisson, M. Pézolet and R. E. Prud'homme, "Orientation and relaxation of orientation of amorphous poly(ethylene terephthalate)," *Polymer,* vol. 42, pp. 9051-9058, 2001.

[19] J. Martin, M. Ponçot, P. Bourson, A. Dahoun and J.-M. Hiver, "Study of the Crystalline Phase Orientation in Uniaxially Stretched Polypropylene by Raman Spectroscopy: Validation and Use of a Time-Resolved Measurement Method," *Polym. Eng. Sci.,* 2011.

[20] M. Ponçot, J. Martin, S. Chaudemanche, O. Ferry, T. Schenk, J.-P. Tinnes, D. Chapron, I. Royaud, A. Dahoun and P. Bourson, "Complementarities of high energy WAXS and Raman spectroscopy measurements to study the crystalline phase orientation in polypropylene blends during tensile test," *Polymer,* vol. 80, pp. 27-37, 2015.

[21] J. B. Faisant de Champchesnel, D. I. Bower, I. M. Ward, J. F. Tassin and G. Lorentz, "Development of molecular orientation in sequentially drawn PET films," *Polymer,* vol. 34, pp. 3763-3670, 1993.

[22] A. Ajji, K. C. Cole, M. M. Dumoulin and J. Brisson, "Amorphous orientation of poly(ethylene terephthalate) by X-ray diffraction in combination with Fourier transform infra-red spectroscopy," *Polymer,* vol. 36, pp. 4023-4030, 1995.

[23] U. Göschel, K. Deutscher and V. Abetz, "Wide-angle X-ray scattering studies using an area detector: crystallite orientation in semicrystalline PET structures," *Polymer,* vol. 37, pp. 1-6, 1996.

[24] L. V. Todorov, C. I. Martins and J. C. Viana, "Solid-State Structural Evolution of Poly(ethylene terephthalate) During Step Uniaxial Stretching from Different Initial Morphologies: An In Situ Wide Angle X-ray Scattering Study," *J. Appl. Polym. Sci.,* vol. 124, pp. 470-483, 2012.

[25] G. Stoclet, R. Seguela, J.-M. Lefebvre and C. Rochas, "New Insights on the Strain-Induced Mesophase of Poly(D,L-lactide): In Situ WAXS and DSC Study of the Thermo-Mechanical

Stability," *Macromolecules,* vol. 43, pp. 7228-7237, 2010.

[26] F. Zuo, J. K. Keum, X. Chen, B. S. Hsiao, H. Chen, S.-Y. Lai, R. Wevers and J. Li, "The role of interlamellar chain entanglement in deformation-induced structure changes during uniaxial stretching of isotactic polypropylene," *Polymer,* vol. 48, pp. 6867-6880, 2007.

[27] M. F. Butler and A. M. Donald, "Deformation of spherulitic polyethylene thin films," *J. Mater. Sci,* vol. 32, pp. 3675-3685, 1997.

[28] J. Wu, J. M. Schultz, J. M. Samon, A. B. Pangelinan and H. H. Chuah, "In situ study of structure development in poly(trimethylene terephthalate) fibers during stretching by simultaneous synchrotron small- and wide-angle X-ray scattering," *Polymer,* vol. 42, pp. 7141-7151, 2001.

[29] E. Gorlier, J. M. Haudin and N. Billon, "Strain-induced crystallization in bulk amorphous PET under uni-axial loading," *Polymer,* vol. 42, pp. 9541-9549, 2001.

[30] D. Kawakami, B. S. Hsiao, S. Ran, C. Burger, B. Fu, I. Sics, B. Chu and T. Kikutani, "Structural formation of amorphous poly(ethylene terephthalate) during uniaxial deformation above glass temperature," *Polymer,* vol. 45, pp. 905-918, 2004.

[31] D. P. Pope and A. Keller, "Deformation of Oriented Polyethylene," *J. Polym. Sci. Polym. Phys. Ed.,* vol. 13, pp. 533-566, 1975.

[32] K. Schneider, S. Trabelski, N. E. Zafeiropoulos, R. Davies, C. Riekel and M. Stamm, "The Study of Cavitation in HDPE Using Time Resolved Synchrotron X-ray Scattering During Tensile Deformation," *Macromol. Symp.,* vol. 236, pp. 241-248, 2006.

[33] M. Vigny, J. F. Tassin and G. Lorentz, "Study of the molecular structure of PET films obtained by an inverse stretching process, Part 2: crystalline reorganization during longitudinal drawing," *Polymer,* vol. 40, pp. 397-406, 1999.

[34] J. M. Samon, J. M. Schultz and B. S. Hsiao, "Study of the cold drawing of nylon 6 fiber by in-situ simultaneous small- and wide-angle X-ray scattering techniques," *Polymer,* vol. 41, pp. 2169-2182, 2000.

[35] H. Guo, J. Wang, C. Zhou, W. Zhang, Z. Wang, B. Xu, J. Li, Y. Shang, J. de Claville Christiansen, D. Yu, Z. Wu and S. Jiang, "Direct investigations of deformation and yield induced structure transitions in polyamide 6 below glass transition temperature with WAXS and SAXS," *Polymer,* vol. 70, pp. 109-117, 2015.

[36] H. Guo, Y. Zhang, F. Xue, Z. Cai, Y. Shang, J. Li, Y. Chen, Z. Wu and S. Jiang, "In-situ synchrotron SAXS and WAXS investigations on deformation and alpha-beta transformation of uniaxial stretched poly(vinylidene fluoride)," *Cryst. Eng. Comm.,* vol. 15, pp. 1597-1606, 2013.

[37] S. Humbert, O. Lame, J. M. Chenal, C. Rochas and G. Vigier, "New Insight on Initiation of Cavitation in Semicrystalline Polymers: In-Situ SAXS Measurements," *Macromolecules,* vol. 43,

pp. 7212-7221, 2010.

[38] Y. Men, J. Rieger and G. Strobl, "Role of the Entangled Amorphous Network in Tensile Deformation of Semicrystalline Polymers," *Phys. Rev. Lett.,* vol. 91, pp. 9-29, 2003.

[39] A. Pawlak and A. Galeski, "Cavitation during Tensile Deformation of Polypropylene," *Macromolecules,* vol. 41, pp. 2839-2851, 2008.

[40] F. Addiego, A. Dahoun, C. G'sell and J.-M. Hiver, "Characterization of volume strain at large deformation under uniaxial tension in high-density polyethylene," *Polymer,* vol. 47, pp. 4387-4399, 2006.

[41] M. Ponçot, F. Addiego and A. Dahoun, "True intrinsic mechanical behaviour of semi-crystalline and amorphous polymers: Influences of volume deformation and cavities shape," *Int. J. Plast.,* vol. 40, pp. 126-139, 2013.

[42] A. Metha, U. Gaur and B. Wunderlich, "Equilibrium Melting Parameters of Poly(ethylene Terephthalate)," *J. Polym. Sci.: Polym. Phys. Ed.,* vol. 16, pp. 289-296, 1978.

[43] R. de P. Daubeny and C. W. Bunn, "The Crystal Structure of Polyethylene Terephthalate," *Proc. R. Soc. A,* pp. 531-542, 1954.

[44] C. G'sell, J.-M. Hiver and A. Dahoun, "Experimental characterization of deformation damage in solid polymers under tension and its interrelation with necking," *Int. J. Solids Struct.,* vol. 39, pp. 3857-3872, 2002.

[45] C. G'sell, J.-M. Hiver, A. Dahoun and A. Souahi, "Video-controlled tensile testing of polymers and metals beyond the necking point," *J. Mater. Sci.,* vol. 27, pp. 5031-5039, 1992.

[46] M. Ponçot, "Comportements thermomécaniques de polymères chargés selon différents chemins de déformation et traitements thermiques," Ph. D. Thesis, INPL, Nancy, 2009.

[47] A. P. Hammersley, "FIT2D: An Introduction and Overview," *ESRF Internal Report,* vol. ESRF97HA02T, 1997.

[48] A. P. Hammersley, S. O. Svensson, M. Hanfland, Fitch A. N. and D. Häusermann, "Two-Dimensional Detector Software: From Real Detector to Idealised Image or Two-Theta Scan," *High Pressure Res.,* vol. 14, pp. 235-248, 1996.

[49] P. H. Hermans and A. Weidinger, "Quantitative X-ray investigations on the crystallinity of cellulose fibers. A background analysis.," *J. Appl. Phys.,* vol. 19, pp. 491-506, 1948.

[50] E. A. Sander and V. H. Barocas, "Comparison of 2D fiber network orientation measurement methods," *J. Biomed. Mater. Res., Part A,* pp. 322-331, 2008.

[51] G. V. Gusev, "Hermans-Weidinger X-ray diffraction technique for determining polymer

crystallinity and the use of the Ruland ratio," *Polym. Sci. U.S.S.R.,* vol. 20, pp. 1295-1297, 1979.

[52] P. Scherrer, *Göttinger Nachrichten Gesell.,* vol. 2, p. 98, 1918.

[53] K. Momma and F. Izumi, "VESTA 3 for the three-dimensional visualization of crystal, volumetric and morphology data," *J. Appl. Crystallogr.,* vol. 44, pp. 1272-1276, 2011.

[54] W. J. Dulmage and A. L. Geddes, "Structure of Drawn Polyethylene Terephthalate," *J. Polym. Sci.,* vol. 31, pp. 499-512, 1958.

[55] R. Séguéla, "Critical review of the molecular topology of semicrystalline polymers: The origin and assessment of intercrystalline tie molecules and chain entanglements," *J. Polym. Sci., Part B: Polym. Phys.,* vol. 43, pp. 1729-1748, 2005.

[56] M. A. Kennedy, A. J. Peacock, M. D. Failla, Lucas J. C. and L. Mandelkern, "Tensile Properties of Crystalline Polymers: Random Copolymers of Ethylene," *Macromolecules,* vol. 28, pp. 1407-1421, 1995.

[57] B. Crist, C. J. Fisher and Howard P. R., "Mechanical Properties of Model Polyethylenes: Tensile Elastic Modulus and Yield Stress," *Macromolecules,* vol. 22, pp. 1709-1718, 1989.

[58] N. W. Brooks, M. Ghazali, R. A. Duckett, A. P. Unwin and I. M. Ward, "Effects of morphology on the yield stress of polyethylene," *Polymer,* vol. 40, pp. 821-825, 1999.

[59] W. J. O'Kane and R. J. Young, "The role of dislocations in the yield of polypropylene," *J. Mater. Sci. Lett.,* vol. 14, pp. 433-435, 1995.

[60] R. J. Young, "Screw Discolocation Model for Yield in Polyethylene," *Mater. Forum,* vol. 11, pp. 210-216, 1988.

[61] A. Bellare, R. E. Cohen and A. S. Argon, "Development of texture in poly(ethylene terephthalate) by plane-strain compression," *Polymer,* vol. 34, pp. 1393-1403, 1993.

[62] K. H. Nitta and M. Takayanagi, "Tensile yield of isotactic polypropylene in terms of a lamellar-cluster model," *J. Polym. Sci., Part B: Polym. Phys.,* vol. 38, pp. 1037-1044, 2000.

[63] R. Séguéla, "Plasticity of semi-crystalline polymers: crystal slip versus melting-recrystallization," *e-Polym.,* no. 32, 2007.

[64] J. Stockfleth, L. Salamon and G. Hinrichsen, "On the deformation mechanisms of oriented PET and PP films under load," *Colloid Polym. Sci.,* vol. 271, pp. 423-435, 1993.

[65] R. J. Rule, D. H. MacKerron, A. Mahendrasingam, C. Martin and T. M. W. Nye, "Time-Resolved Two-Dimensional Small Angle X-Ray Scattering Studies of Oriented Poly(ethylene terephthalate) (PET) Using Paracrystalline Modeling Techniques," *Macromolecules,* vol. 28, pp. 8517-8522, 1995.

[66] N. S. Murthy and D. T. Grubb, "Deformation in Lamellar and Crystalline Structures: in-situ Simultaneous Small-Angle X-ray Scattering and Wide-Angle X-ray Diffraction Measurements on Polyethylene Terephthalate Fibers," *J. Polym. Sci., Part B: Polym. Phys.,* vol. 41, pp. 1538-1553, 2003.

[67] N. S. Murthy and D. T. Grubb, "Tilted Lamellae in an Affinely Deformed 3D Macrolattice and Elliptical Features in Small-Angle Scattering," *J. Polym. Sci., Part B: Polym. Phys.,* vol. 44, pp. 1277-1286, 2006.

[68] W. Wang, N. S. Murthy and D. T. Grubb, "'Butterfly' small-angle X-ray scattering patterns in semicrystalline polymers are double-elliptical," *Polymer,* vol. 48, pp. 3393-3399, 2007.

Highlights

- A combined analysis of SAXS and WAXS data for the study of deformation micromechanisms.
- Measurement of macromolecular orientation, 3D lamellae size and shape.
- The description and application of a new method to follow macromolecular orientation.
- Emphasis on several deformation mechanisms in semi-crystalline polymers.